Supplementary Note 8: Simulation of the effect of a half–unit-cell offset shift on EMCD map measurement in $DyFeO_3$

In order to exclude the possibility of artifacts arising from the presence of a half–unit-cell offset in $DyFeO_3$ during EMCD map extraction, as described in Extended Data Fig. 5, a simulation test was performed in which the total EELS signal maps were artificially shifted by half a unit cell and then realigned (**Fig. S8,** upper panel). The resulting subtracted maps retained clear atomic contrast and reproduced the expected antiferromagnetic ordering pattern, confirming that our data processing workflow does not introduce artifacts, which could mimic magnetic order. We also constructed two total EELS signal maps excluding the magnetic contribution (**Fig. S8**, lower panel). The corresponding EMCD difference map exhibits very weak signals, in stark contrast to the upper panel, in which the magnetic contribution is retained. The residual signals arise from minor misalignments between the two stacks shifted by half a unit cell. Importantly, the weak residual signals are localized at the Fe atomic columns and are different from the alternating contrast characteristic of antiferromagnetic ordering.

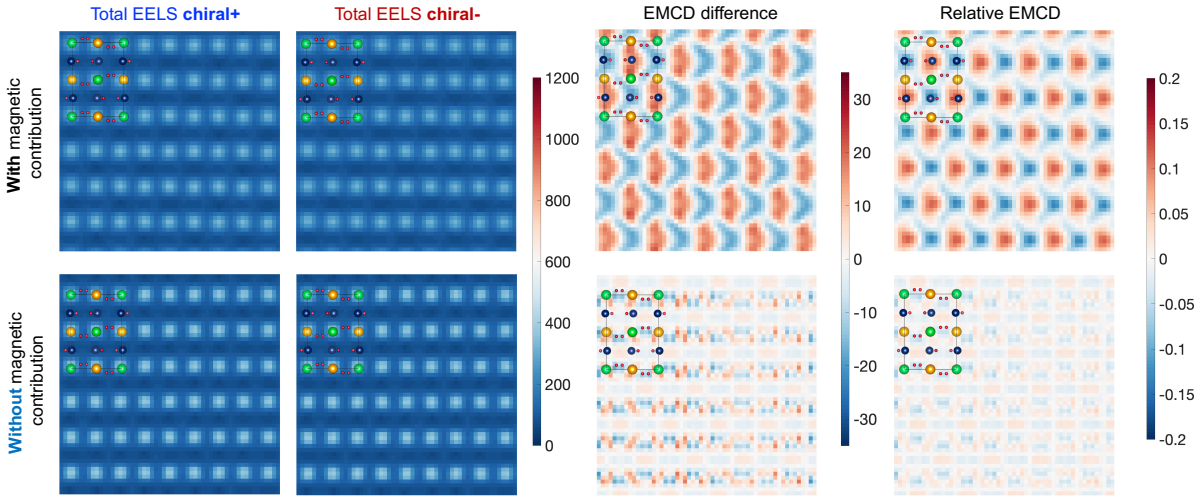


Fig. S8 | Simulation test of the effect of a half–unit-cell offset shift on EMCD signal extraction. Simulated total EELS signal maps for the *chiral+* and *chiral-* (shifted by half a unit cell with respect to *chiral+*) are shown in the left two columns. The corresponding EMCD difference and relative EMCD maps are shown in the right two columns. Upper panels: results obtained with the magnetic contribution, in which the EMCD maps preserve clear atomic magnetic contrast and reproduce the expected antiferromagnetic ordering pattern. Lower panels: results obtained without the magnetic contribution, showing very weak residual signals arising from minor misalignment between the two artificially-shifted stacks. The weak signals are localized at the Fe atomic columns (atomic model overlaid) and are clearly distinguishable from the alternating contrast characteristic of antiferromagnetic order.

Supplementary Note 9: Alternative approach for the extraction of EMCD signals at the $SmFeO_3$-$DyScO_3$ interface

This alternative approach, which is described in the Methods section, is used to extract EMCD signals at the $SmFeO_3$–$DyScO_3$ interface. It avoids subtracting two chiral EELS stacks shifted by half a unit cell. The extracted EMCD maps, which are displayed in **Fig. S9**, are consistent with the results shown in Fig. 4 of the main text, which used a half-unit-cell shift.

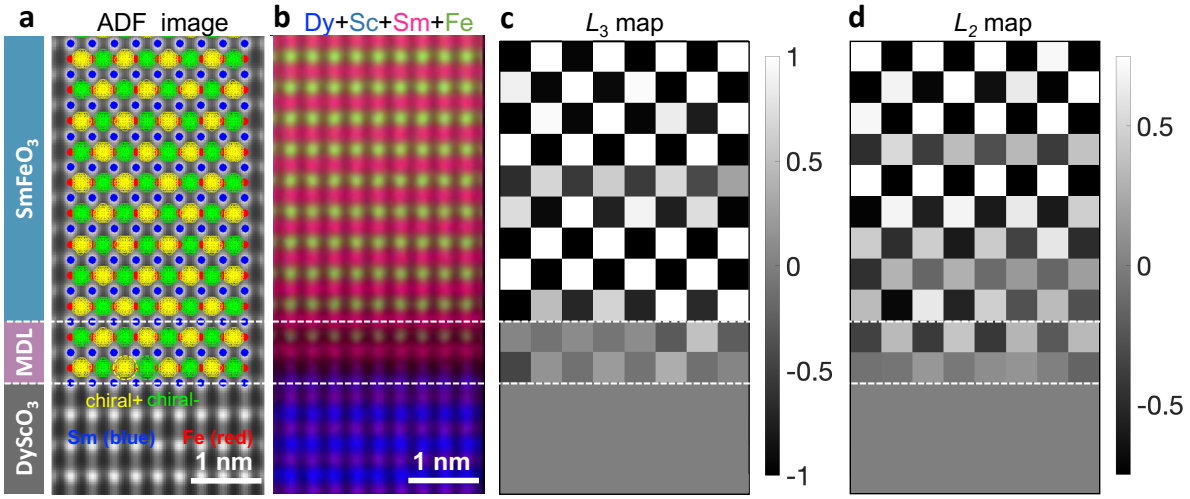


Fig. S9 | Extraction of EMCD signals at the $SmFeO_3$-$DyScO_3$ interface without applying the half-unit-cell shift described in Extended Data Fig. 5. a, ADF image across the interface after template matching. Sm (blue) and Fe (red) atomic columns are marked using corresponding colored dots. The chiral+ and chiral- regions used for chiral EELS signal extraction are indicated by yellow and green circles, respectively. **b,** Combined elemental maps for Dy (blue), Sc (violet), Sm (pink) and Fe (green) across the interface. **c,d,** EMCD maps at the L_3 and L_2 edges obtained by comparing the chiral EELS signals with the mean Fe *L*-edge spectrum.

References

1. Song, D. & Dunin-Borkowski, R. E. Three-Dimensional Measurement of Magnetic Moment Vectors Using Electron Magnetic Chiral Dichroism at Atomic Scale. *Phys. Rev. Lett.* **127**, 087202 (2021).
2. Song, D. *et al.* An in-plane magnetic chiral dichroism approach for measurement of intrinsic magnetic signals using transmitted electrons. *Nat Commun* **8**, 15348 (2017).
3. Rusz, J., Rubino, S., Eriksson, O., Oppeneer, P. M. & Leifer, K. Local electronic structure information contained in energy-filtered diffraction patterns. *Phys. Rev. B* **84**, 064444 (2011).
4. Cui, J., Sha, H., Yang, W. & Yu, R. Antiferromagnetic imaging via ptychographic phase retrieval. *Science Bulletin* **69**, 466–472 (2024).

Despite its potential for atomic-scale magnetic imaging of antiferromagnets, EMCD faces two main obstacles: low signal-to-noise ratio (SNR) due to weak inelastic signals from an *off-axis* experimental setup[9] and spatial resolution limited to atomic planes by its three-beam diffraction geometry[10–12].

In this paper, we introduce an atomic-column-resolved EMCD technique implemented in a standard STEM-EELS[13–15] setup on a commercially-available aberration-corrected scanning TEM (STEM). Our redesigned diffraction geometry preserves atomic-column resolution by operating on-zone-axis and enahnces signal intensity by an order of magnitude through *on-axis* acquisition compared with conventional *off-axis* setups. Applying to antiferromagnets $DyFeO_3$ and α-Fe_2O_3, we resolve their distinct G-type and C-type antiferromangtic orderings at the atomic-column level. We further map the magnetic dead layer at the buried $DyScO_3$-$SmFeO_3$ interface, revealing a one-unit-cell-thick region of suppressed magnetism while the antiferromagnetic coupling remains intact.

Principle of atomic-column EMCD

Fig. 1a shows the experimental setup for atomic-column EMCD in a STEM. An atomic-sized electron probe passes through an antiferromagnetic crystal, in which inelastic scattering occurs as electrons interact with the magnetic atoms, exciting transitions such as those from 2*p* to unoccupied 3*d* orbitals at the Fe $L_{3,2}$ edge. In standard STEM-EELS setup, an annular dark-field (ADF) detector is used to collect high-angle-scattered electrons to image atomic columns, while an EEL spectrometer records inelastic scattering signals simultaneously by using an *on-axis* EELS aperture in the diffraction plane to generate a spectrum on a digital detector. For a magnetic crystal, in which time-reversal symmetry is broken, the EELS signal contains both nonmagnetic and magnetic (EMCD) components[16,17]. By analyzing the distribution of these signals in the diffraction plane, the EMCD signals can be isolated.

Conventional EMCD signals are obtained under a three-beam geometry by measuring *off-axis* chiral EELS signals at two conjugate positions in the diffraction plane[6], where the EMCD signals are dispersed across four quadrants with low intensity. Considering the chirality around individual magnetic atomic columns, which is absent in nonmagnetic ones, EELS signals are also chiral across magnetic atoms and EMCD signals can be extracted in real space[18]. To verify this, we take the example of antiferromagnetic orthoferrite $DyFeO_3$, which has a G-type spin configuration (Fig. 1b). The Fe spins form a regular pattern of alternating magnetic ordering across the entire lattice[19]. The atomic model is projected along the *z* direction (zone-axis geometry) and the spins are oriented along the *x* axis. We placed the electron probe at two symmetrical positions around a magnetic atom column, as marked by stars in Fig. 1b. We then simulated the distribution of nonmagnetic and magnetic signals in the diffraction plane (Fig. 1c-e). The dashed circle marks the position of the *on-axis* EELS entrance aperture used for signal acquisition.

When the electron probe is positioned on the center of an atomic column (marked by blue star), the EMCD signal distributions are antisymmetric in the diffraction plane, resulting in a net zero magnetic signal in the *on-axis* EELS aperture (Fig. 1d). At two symmetrical positions that are offset from the atomic column (marked by black and red stars), the nonmagnetic signal is symmetric with respect to the center of the diffraction plane (Fig. 1c), and the integrated signal in the aperture remains unchanged. In contrast, the magnetic signals are antisymmetric and the sign of the integrated signal is reversed (Fig. 1d). Therefore, the EMCD signals can be obtained by subtracting the total chiral EELS signals (Fig. 1e) from the two symmetrical positions around the magnetic atom columns, as schematically shown in Fig. 1f for the Fe $L_{3,2}$ edges. By using this approach, the entire magnetic lattice can be scanned to generate a three-dimensional (3D) data cube, in which the *x* and *y* axes are real-space positions (Fig. 1g). By extracting the EMCD signals from each atomic column, the magnetic ordering can be mapped with atomic-

column lateral resolution. Noted that the spins here are oriented *perpendicular* to the electron beam direction[18,20], unlike in conventional EMCD where they are *parallel* to the electron beam[6]. This configuration localizes the magnetic signal around the directly transmitted electron beam, enabling the use of an *on-axis* EELS acquisition setup and the enhancement of signal intensity (Supplementary Note 1 and Fig. S1).

Imaging antiferromagnetic order in $DyFeO_3$

We simulated EMCD signals for G-type $DyFeO_3$ with atomic-column resolution (see Methods for details) for an electron probe that was scanned across the entire atomic model shown in Fig. 2a. The electron beam was aligned along the *z* axis and the Fe spins were oriented along the *x* axis at room temperature. The Néel temperature of $DyFeO_3$ is T_N = 645 K. The magnetic moment of Dy is quenched at room temperature (T_N^{Dy} = 4.5 K)[19] and is therefore neglected here. For each scanning point in the supercell, the nonmagnetic and magnetic EMCD signals in the diffraction plane were calculated. The simulation was performed for an accelerating voltage of 300 kV, a beam convergence semi-angle of 17.8 mrad and a sample thickness of 22.38 nm. Diffraction patterns for each scanning point are provided in Extended Data Fig. 1. The simulated real-space distributions of the EMCD signals are shown in Fig. 2b for Fe (Supplementary Note 2 and Fig. S2). The atomic-column-resolved EMCD signals are clearly distinguishable with an alternating pattern, showing a localized distribution between the Fe atomic columns, as indicated by the overlaid atomic model. We define the chiral+ and chiral- positions in Fig. 2b. By subtracting the EELS signals at these two chiral positions, the EMCD signal from the individual atomic columns can be isolated. Since the experimental conditions affect EMCD signals significantly[18,21], we also calculated the EMCD intensity as a function of convergence semi-angle and sample thickness (Extended Data Fig. 2). We found that the

Content

Table of Contents

Supplementary Note 1: Comparison of signal intensity using on-axis and off-axis setups ..2

Supplementary Note 2: Details of the simulation of EMCD signals in $DyFeO_3$ 4

Supplementary Note 3: Separation of EMCD signals from three orthogonal magnetization directions.....6

Supplementary Note 4: EMCD signals for Dy.....8

Supplementary Note 5: EMCD spectra across the $DyScO_3$-$SmFeO_3$ interface.....10

Supplementary Note 6: Dose dependence of EMCD signals.....11

Supplementary Note 7: Effect of beam misorientation on EMCD signals.....13

Supplementary Note 8: Simulation of the effect of a half–unit-cell offset shift on EMCD map measurement in $DyFeO_3$.....15

Supplementary Note 9: Alternative approach for the extraction of EMCD signals at the $SmFeO_3$-$DyScO_3$ interface.....16

Supplementary Note 1: Comparison of signal intensity using *on-axis* and *off-axis* setups

In the conventional EMCD geometry, with the sample magnetization oriented along the *z*-axis (parallel to the electron beam), the EMCD signals are always localized away from the transmitted beam, a characteristic observed under both three-beam and zone-axis conditions. In such configurations, an *off-axis* aperture (yellow rectangle marked in **Fig. S1a**) is typically used to selectively collect the EELS signals. In contrast, in our approach the magnetization is oriented along the *x*-axis or *y*-axis, resulting in EMCD signals that are concentrated around the transmitted beam. This configuration allows for the use of an *on-axis* aperture (yellow circle marked in **Fig. S1e**) for EELS signal collection. In order to make a quantitative comparison, we calculated the nonmagnetic (**Fig. S1b** and **S1f**) and magnetic (**Fig. S1c** and **S1g**) signal components across the entire unit cell of $DyFeO_3$ using the aperture configurations shown in **Fig. S1a** and **S1e**. The total EELS signal, obtained by summing the nonmagnetic and magnetic contributions, is shown in **Fig. S1d** and **S1h**. **Fig. S1i** presents the ratio of total signal intensities between the *on-axis* and *off-axis* configurations. Our *on-axis* approach yields a significantly stronger total signal - enhanced by more than an order of magnitude - compared to the conventional *off-axis* approach. This efficient collection of the localized magnetic signal directly leads to a marked improvement in SNR.

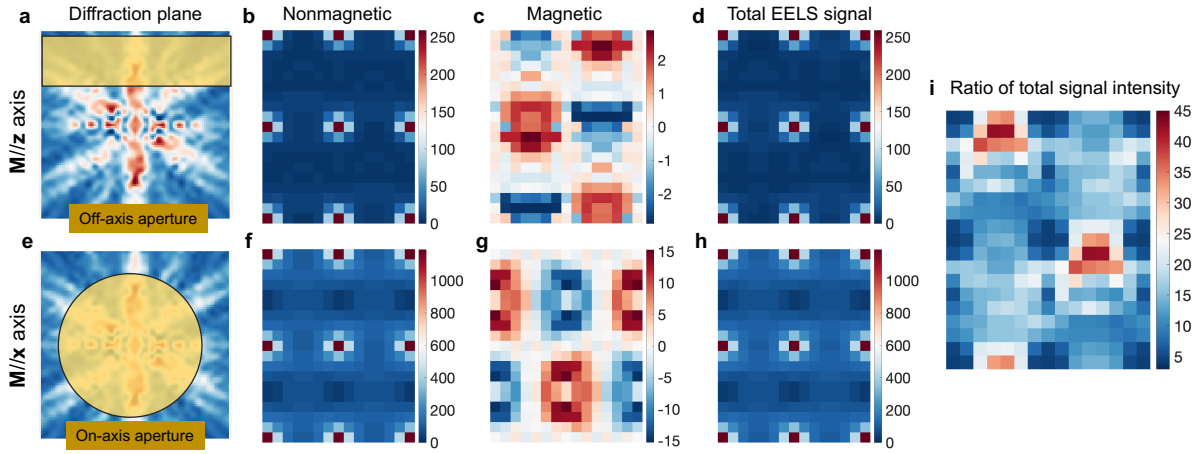


Fig. S1 | Comparison of signal intensity using *on-axis* and *off-axis* apertures. a, e, Schematic diagrams showing the positions of the EELS collection aperture for obtaining EMCD signals with the magnetization oriented along the *z* and *x* directions, respectively. **b-d**, Real-space maps of the simulated nonmagnetic, magnetic and total signals across the $DyFeO_3$ unit cell, assuming that the magnetization lies along the *z* direction (conventional EMCD diffraction geometry). **f-h**, As for **b-d**, but assuming that the magnetization lies along the *x* direction (this work). **i**, Ratio of total signal intensity between **d** and **h**.

Supplementary Note 2: Details of the simulation of EMCD signals in $DyFeO_3$

The antiferromagnetic $DyFeO_3$ structure consists of two magnetic Fe sublattices with opposite spin orientations, i.e., $\overrightarrow{Fe}$ and $\overleftarrow{Fe}$. In our simulations, we take advantage of the ability to separately calculate the nonmagnetic and magnetic scattering contributions for each sublattice. Specifically, we define them as follows:

- $N(\overrightarrow{Fe})$ and $N(\overleftarrow{Fe})$ represent the nonmagnetic signals from the two Fe sublattices,
- $M(\overrightarrow{Fe})$ and $M(\overleftarrow{Fe})$ represent the magnetic signals from the two Fe sublattices.

The relative EMCD signals for each spin orientation are calculated as:

- $EMCD(\overrightarrow{Fe})$ in **Fig. S2** (upper panel): $M(\overrightarrow{Fe}) / (N(\overrightarrow{Fe}) + N(\overleftarrow{Fe}))$
- $EMCD(\overleftarrow{Fe})$ in **Fig. S2** (middle panel): $M(\overleftarrow{Fe}) / (N(\overrightarrow{Fe}) + N(\overleftarrow{Fe}))$

Because the two Fe sublattices have opposite spin orientations, the final EMCD signal ($EMCD(\overrightarrow{Fe})$ - $EMCD(\overleftarrow{Fe})$), which is shown in **Fig. S2** (lower panel), is obtained by subtracting the two spin-oriented signals:

$(M(\overrightarrow{Fe}) - M(\overleftarrow{Fe})) / (N(\overrightarrow{Fe}) + N(\overleftarrow{Fe}))$.

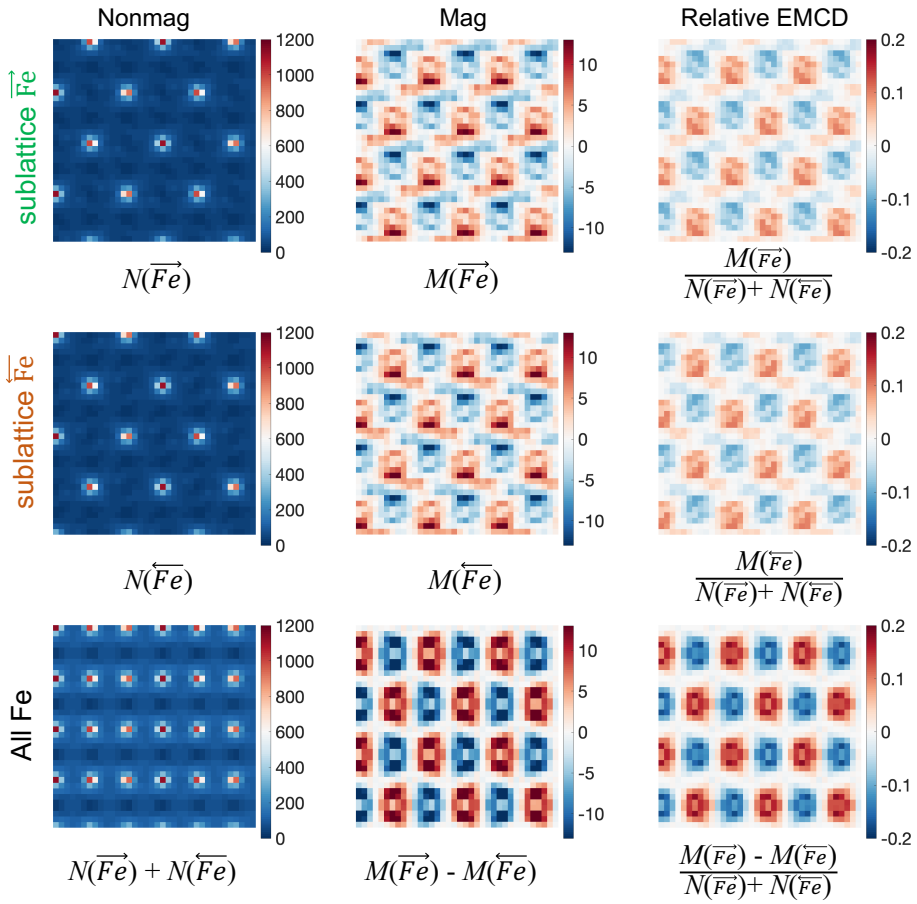


Fig. S2 | Simulated real-space distributions of nonmagnetic, magnetic and relative EMCD signals. Shown from left to right are simulated maps of nonmagnetic, magnetic and relative EMCD signals in real space. The upper, middle and lower panels correspond to Fe sublattice $\overrightarrow{Fe}$, Fe sublattice $\overleftarrow{Fe}$ and combined Fe lattice, respectively. Specifically, $N(\overrightarrow{Fe})$ and $N(\overleftarrow{Fe})$ denote nonmagnetic signals from the two Fe sublattices, while $M(\overrightarrow{Fe})$ and $M(\overleftarrow{Fe})$ represent their corresponding magnetic signals. The relative EMCD signals for each spin orientation are calculated as $EMCD(\overrightarrow{Fe}) = M(\overrightarrow{Fe}) / (N(\overrightarrow{Fe}) + N(\overleftarrow{Fe}))$ and $EMCD(\overleftarrow{Fe}) = M(\overleftarrow{Fe}) / (N(\overrightarrow{Fe}) + N(\overleftarrow{Fe}))$. Because the two Fe sublattices have opposite spin orientations, the total EMCD signal $EMCD(\overrightarrow{Fe})$ - $EMCD(\overleftarrow{Fe})$ is obtained as $(M(\overrightarrow{Fe}) - M(\overleftarrow{Fe})) / (N(\overrightarrow{Fe})+ N(\overleftarrow{Fe}))$, corresponding to the result shown in **Fig. 2b**.

Supplementary Note 3: Separation of EMCD signals from three orthogonal magnetization directions

EMCD can be used to measure magnetic signals in three spatial directions on the nanometer scale, as EMCD signals arising from magnetization in the three Cartesian directions have distinct distributions in the diffraction plane[1–3]. This principle applies to both atomic-plane resolution and atomic-column resolution measurements. In the present study, we calculated the distribution of EMCD signals assuming that the magnetic vector is oriented along the *x*, *y* or *z* directions, as shown for $DyFeO_3$ in Extended Data Fig. 6a-d. By integrating the EMCD signals over the *on-axis* EELS aperture in the diffraction plane, one can visualize the real-space distribution of both nonmagnetic and magnetic EMCD signals for the three spin configurations in Extended Data Fig. 6e-h. The nonmagnetic signals remain unchanged, as they are independent of the spin configuration.

For spins oriented along the *x* axis, which represents a real magnetic configuration, the EMCD signals are localized between the Fe columns along the *y* direction, almost coinciding with the positions of the Dy columns. These signals exhibit an alternating pattern, with reversed signs. When the spins are oriented along the *y* axis, the EMCD signals are localized between the Fe columns along the *x* direction, showing a distinct distribution. For spins oriented along the *z* axis, the situation is similar to that for conventional EMCD, being sensitive only to magnetization along the electron beam direction (*z* axis). In this case, the EMCD signals exhibit an antisymmetric distribution in the diffraction plane, contributing to negligible or zero signals when using an *on-axis* EELS aperture, as shown in Extended Data Fig. 6h. Therefore, these signals can be neglected here.

The separation of EMCD signals from different directions is crucial for rigorously validating the feasibility of our method. For $DyFeO_3$, real-space maps of simulated EMCD signals across a unit cell are shown in **Fig. S3a-c**, assuming that the magnetization lies along the *x*, *y* and *z* directions, respectively. When the spins are oriented along the *x*-axis, the EMCD signals are localized primarily at the Dy sites (**Fig. S3a**). Corresponding line profiles (**Fig. S3d**) extracted from the blue rectangular region indicated in **Fig. S3a-c** reveal significant variations in EMCD intensity across atomic columns. For comparison, EMCD signals for the *y*- and *z*-oriented magnetizations are plotted in **Fig. S3d**. The *x*-component signal is more than an order of magnitude stronger at its characteristic Dy sites compared to the other two directions. Similarly, when the spins are oriented along the *y*-axis, the EMCD signals are localized between Fe sites (**Fig. S3b**). The line profiles in **Fig. S3e**, which are extracted from the black rectangular region

in **Fig. S3a-c**, confirm that the signals from the *x*- and *z*-oriented magnetizations are negligible compared to the signal from the *y*-direction. This quantitative analysis highlights the distinct spatial localization of the magnetic contributions and provides evidence for their separability at the atomic scale.

In our experiments, the EMCD signal maps shown in Fig. 2e-f are in good agreement with the results derived for spins along the *x* axis, as shown in Extended Data Fig. 6b and 6f. These results not only confirm the *x*-oriented spin configuration, but also demonstrate that atomic-column EMCD is able to resolve magnetic ordering without requiring prior magnetic information about the crystal, thereby showcasing its ability to resolve magnetic structure. Furthermore, to rule out EMCD signals arising from the spins oriented along the *y* axis, we summed the signals at the chiral+ and chiral- positions, as defined in Extended Data Fig. 6g for the *y*-oriented spin configuration. These chiral positions are also indicated in Extended Data Fig. 7 for the experimental ADF image. The extracted chiral+ and chiral- EELS signals, which are displayed in Extended Data Fig. 7 along with their difference, show negligible EMCD signals. This analysis further confirms that the spin orientation is along the *x* axis.

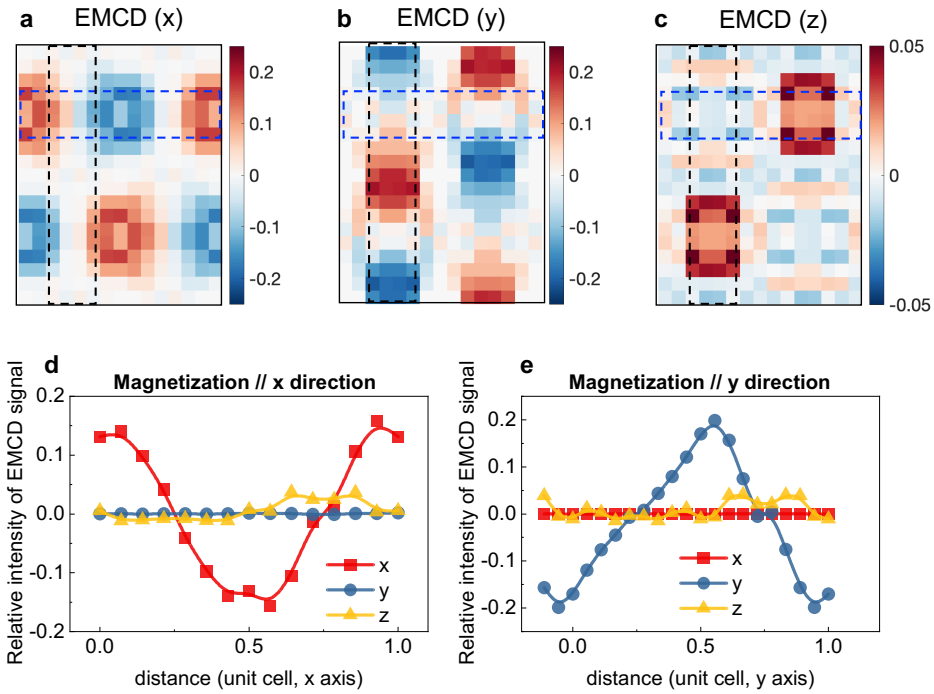


Fig. S3 | Separation of EMCD signals along orthogonal magnetization directions. a-c, Real-space maps of simulated EMCD signals across a unit cell of $DyFeO_3$, assuming magnetization along the *x*, *y* and *z* directions, respectively. **d,** Line profiles extracted from the blue rectangular region indicated in **a-c**. **e,** Line profiles extracted from the black rectangular region indicated in **a-c**.

Supplementary Note 4: EMCD signals for Dy

In $DyFeO_3$, Dy possesses a large intrinsic magnetic moment, but its magnetic ordering temperature is well below room temperature. Consequently, no detectable EMCD signals are expected from Dy in the experiments. In order to verify this behavior, we performed additional analysis focused on the element Dy. In the magnetically-ordered state, the Dy moments are aligned along the *x*-axis and exhibit antiferromagnetic coupling between adjacent *c*-planes, as illustrated in **Fig. S4a**. In this configuration, the EMCD signal is expected to be localized between Dy atomic planes, similar to the case for Fe_2O_3 in **Fig. 3**. We integrated the EELS signals from regions between two Dy atomic planes, as shown schematically in **Fig. S4c**, which corresponds to the line intensity profiles extracted from the ADF image in **Fig. S4b**. The red and green regions indicate chiral+ and chiral- positions, respectively. The resulting chiral EELS signals and their difference (after background removal and post-edge normalization) for the Dy $M_{5,4}$ edges are presented in **Fig. S4d**. No statistically significant EMCD signal is observed for Dy. This null result contrasts with the strong and reproducible EMCD signals obtained from the Fe sublattice (**Fig. 2** in the main text), which remains magnetically ordered at room temperature.

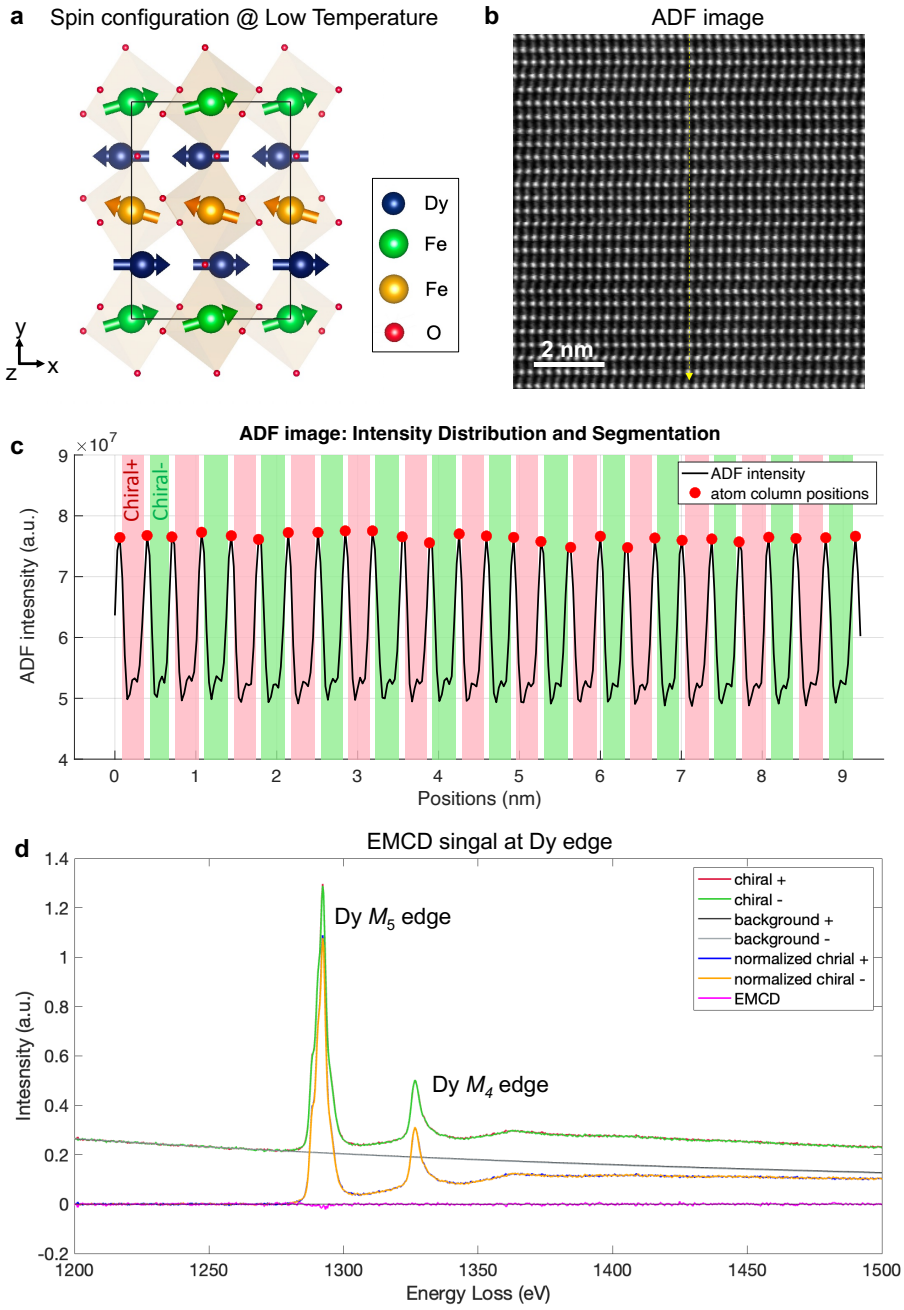


Fig. S4 | EMCD signals for Dy in $DyFeO_3$. a, Atomic model showing the spin configuration of $DyFeO_3$ below the Dy magnetic ordering temperature. **b**, ADF image of $DyFeO_3$ from the same STEM-EELS dataset as in **Fig. 2**. **c**, Line intensity profiles extracted from the ADF image in **b**, with the *chiral+* and *chiral-* regions indicated by red and green rectangles, respectively. **d**, Summed chiral EELS spectra from the *chiral+* and *chiral-* regions, along with their difference.

Supplementary Note 5: EMCD spectra across the $DyScO_3$-$SmFeO_3$ interface

Atomic-column resolved EMCD spectra across the $DyScO_3$–$SmFeO_3$ interface are shown in **Fig. S5**, with the layer numbers indicated in Fig. 4 of the main text. The EMCD spectra for each layer are plotted together.

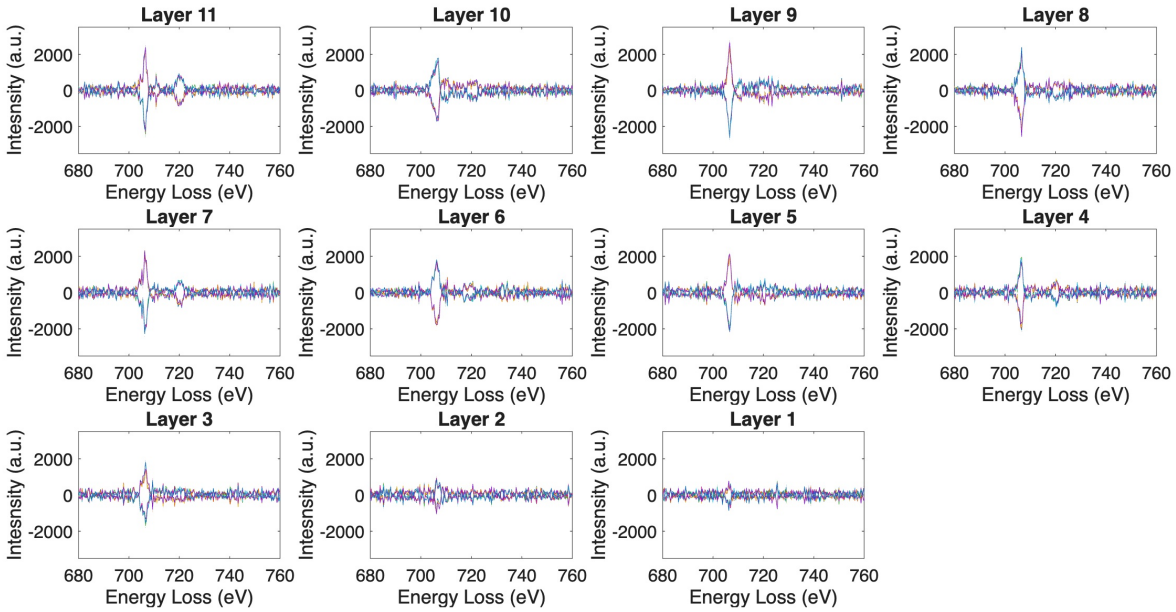


Fig. S5 | Extracted EMCD signals for each atomic column at different layers across the interface. The layer numbers are labelled in Fig. 4. The EMCD signals from columns 1 to 8 at each layer are plotted in the same panel.

Supplementary Note 6: Dose dependence of EMCD signals

To minimize electron beam damage and sample drift, short acquisition times were used for each EELS spectrum over a large area during the STEM–EELS experiments. Based on the typical experimental parameters (beam current: 60 pA, pixel size: 0.325 Å, pixel dwell time: 3 ms), the electron dose for the $DyFeO_3$ measurements is estimated to be approximately 1.06×10^7 $e^-/Å^2$. However, this dose is insufficient to obtain reliable EMCD signals with a high SNR. In order to improve the SNR, a template matching method was applied. An analysis of the SNR of the EMCD signals with respect to the region size used for template matching is shown in **Fig. S6**. The SNR, which is defined as the ratio of the averaged Fe L_3-edge intensity to the standard deviation in the post-edge region (750 - 800 eV), is plotted in **Fig. S6a-c** as a function of the number of templates or integrated area. Representative EELS and EMCD signals are presented in **Fig. S6d-i**. It is evident that an SNR greater than 3 is achieved when 150 templates (corresponding to an integrated area of 5.2 nm × 5.2 nm) are used, enabling the reliable detection of EMCD signals (**Fig. S6e**). Accordingly, the effective electron dose required for atomic-scale EMCD measurement in $DyFeO_3$ is approximately 1.6×10^9 $e^-/Å^2$. The required region size could be further reduced by increasing the beam current and pixel dwell time, provided that the sample damage threshold allows it. We have also estimated the effective electron dose for Fe_2O_3 (Fig. 3). With the experimental parameters (beam current: 30 pA, pixel size: 0.325 Å, pixel dwell time: 1 ms), the estimated effective electron dose is approximately 1.8×10^8 $e^-/Å^2$ (corresponding to an integrated area of 2 nm × 2 nm), which is nearly an order of magnitude lower than that for $DyFeO_3$.

With regard to the comparison with electron ptychography, a much lower electron dose of 9.0×10^5 $e^-/Å^2$ was used[4]. The difference arises because electron ptychography is inherently dose-efficient. However, it requires extremely high phase precision to separate the weak magnetic signal from the dominant electrostatic contribution. In contrast, EMCD relies on the use of inelastically scattered electrons, for which the signal intensity decreases exponentially with increasing energy loss.

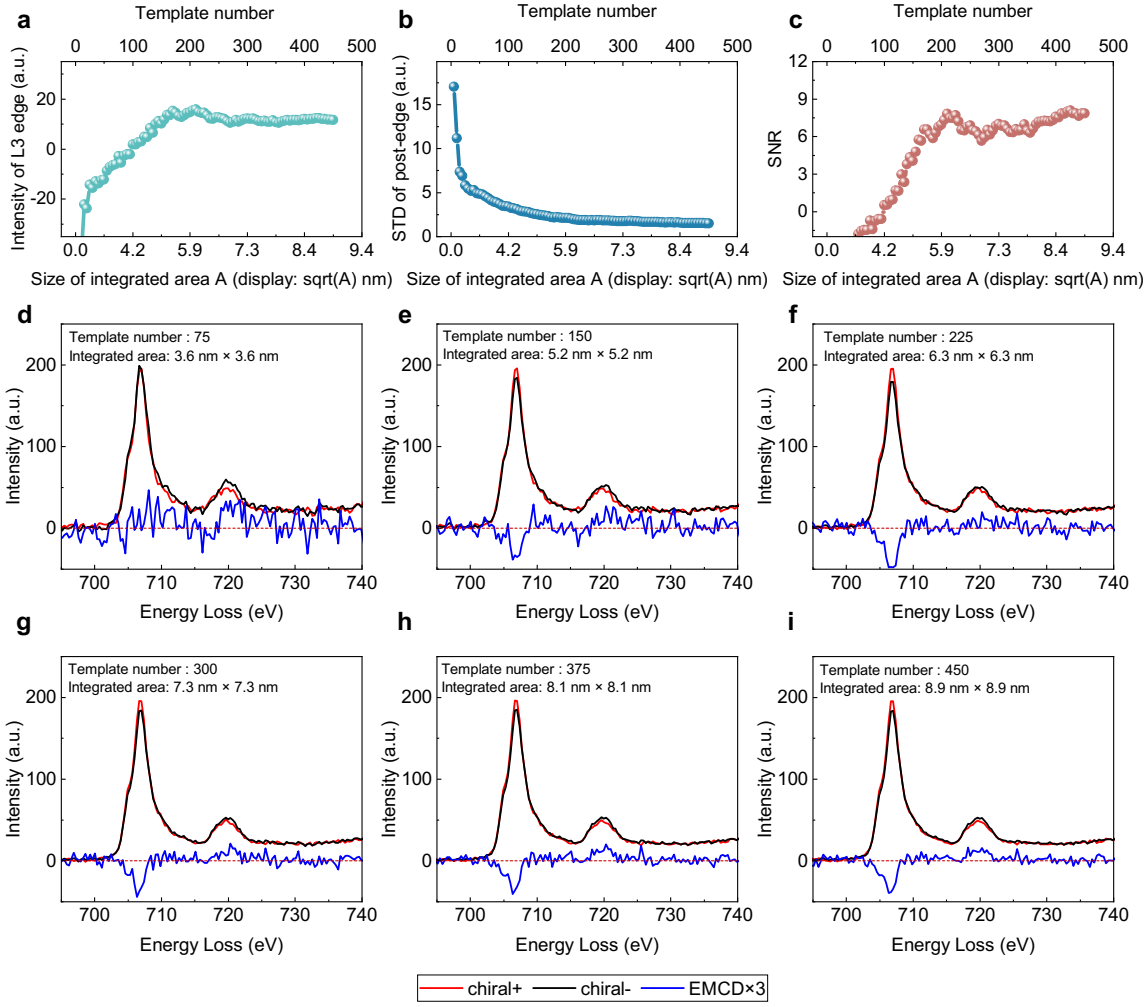


Fig. S6 | Dose dependence of EMCD signals. a, Average Fe L_3 edge intensity plotted *versus* template number and integrated area. The integrated area A is plotted as $\sqrt{A}$ on the x-axis. **b,** Standard deviation (STD) of the EMCD signal intensity in the post-edge region (750-800 eV) plotted *versus* template number and integrated area. **c,** Signal-to-noise ratio (SNR) plotted as a function of template number and integrated area. **d-i,** Representative chiral EELS and corresponding EMCD difference signals at template numbers 75, 150, 225, 300, 375 and 450, corresponding to electron doses of 8×10^8 e$^-$/Å^2, 1.6×10^9 e$^-$/Å^2, 2.4×10^9 e$^-$/Å^2, 3.2×10^9 e$^-$/Å^2, 4.0×10^9 e$^-$/Å^2 and 4.8×10^9 e$^-$/Å^2, respectively.

Supplementary Note 7: Effect of beam misorientation on EMCD signals

In conventional two-beam or three-beam EMCD setups, it is well established that the diffraction conditions strongly influence the distribution of magnetic signals in the diffraction plane, affecting both signal acquisition and reliable extraction. Therefore, it is important to evaluate how beam misorientation impacts real-space EMCD maps in the zone-axis geometry. In order to investigate this question, we performed simulations for $DyFeO_3$ with controlled beam tilts ranging from 0 to 5 mrad. This angular range can be routinely achieved in experiments using PACBED patterns. For simplicity, the tilt was applied independently along the *x*- and *y*-axes.

Fig. S7a-c shows real-space EMCD maps for tilt angles of X = 0, 3 and 5 mrad, while **Fig. S7d-f** shows corresponding results for Y = 0, 3 and 5 mrad. As the beam misorientation increases, the spatial distribution of the EMCD signals in real space remains nearly unchanged, with only a slight reduction in overall intensity observed for tilts up to 5 mrad. The integrated EMCD signal within the region marked by the red rectangle in **Fig. S7a** is plotted as a function of tilt angle, showing minimal variation within this range. However, when the tilt exceeds approximately 7 mrad, the simulations reveal a more pronounced degradation in signal strength. These results demonstrate that the zone-axis EMCD geometry is robust against beam misorientation, maintaining stable signal strength and spatial distribution for tilt variations up to 5 mrad in $DyFeO_3$. This tolerance is significantly broader than that for the conventional three-beam configuration, which typically requires sub-milliradian alignment to preserve signal integrity. This robustness arises from the high symmetry of the zone-axis geometry and from the use of an *on-axis* aperture, which compensates for asymmetries in the signal distribution in the diffraction plane.

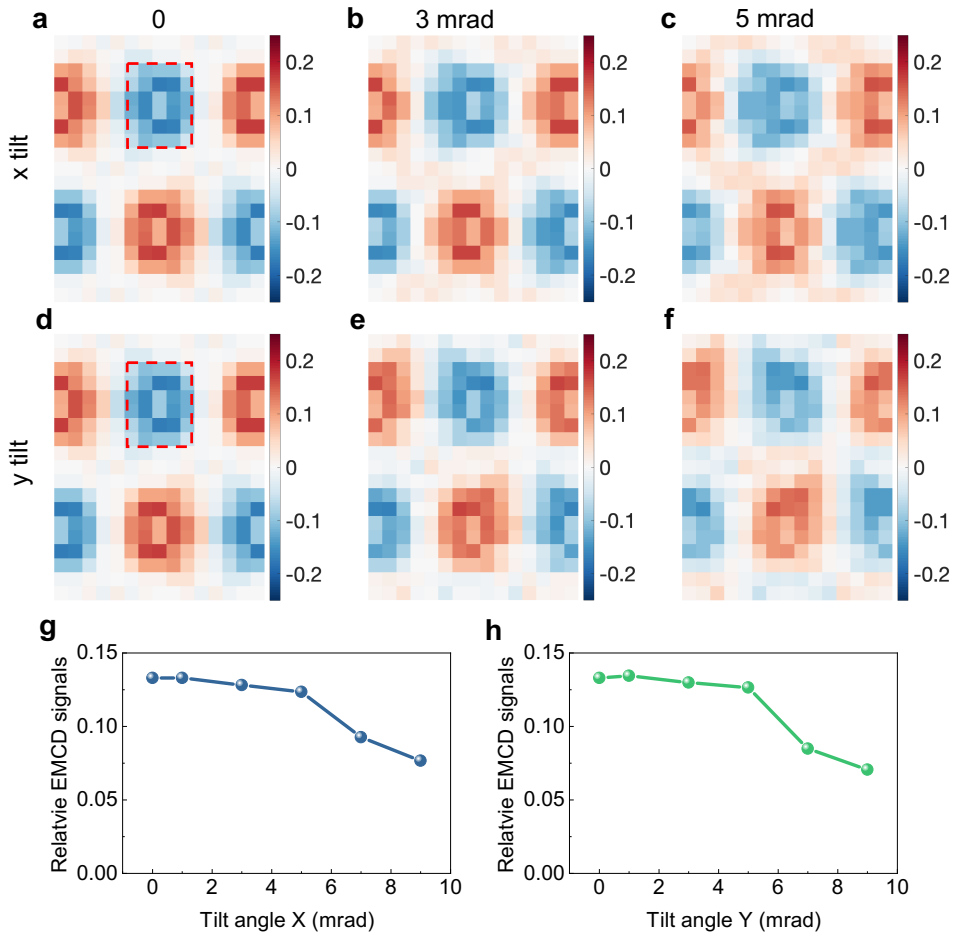


Fig. S7 | Effect of beam tilt on EMCD signals in $DyFeO_3$. a-c, Simulated real-space EMCD maps for beam tilts of $X = 0$, 3, and 5 mrad. **d-f**, Simulated real-space EMCD maps for beam tilts of $Y = 0$, 3, and 5 mrad. **g, h**, Integrated EMCD intensity in the region marked by the red rectangle in **a** and **d**, plotted as a function of the X- and Y-tilt angles, respectively.

Supplementary Note 8: Simulation of the effect of a half–unit-cell offset shift on EMCD map measurement in $DyFeO_3$

In order to exclude the possibility of artifacts arising from the presence of a half–unit-cell offset in $DyFeO_3$ during EMCD map extraction, as described in Extended Data Fig. 5, a simulation test was performed in which the total EELS signal maps were artificially shifted by half a unit cell and then realigned (**Fig. S8,** upper panel). The resulting subtracted maps retained clear atomic contrast and reproduced the expected antiferromagnetic ordering pattern, confirming that our data processing workflow does not introduce artifacts, which could mimic magnetic order. We also constructed two total EELS signal maps excluding the magnetic contribution (**Fig. S8**, lower panel). The corresponding EMCD difference map exhibits very weak signals, in stark contrast to the upper panel, in which the magnetic contribution is retained. The residual signals arise from minor misalignments between the two stacks shifted by half a unit cell. Importantly, the weak residual signals are localized at the Fe atomic columns and are different from the alternating contrast characteristic of antiferromagnetic ordering.

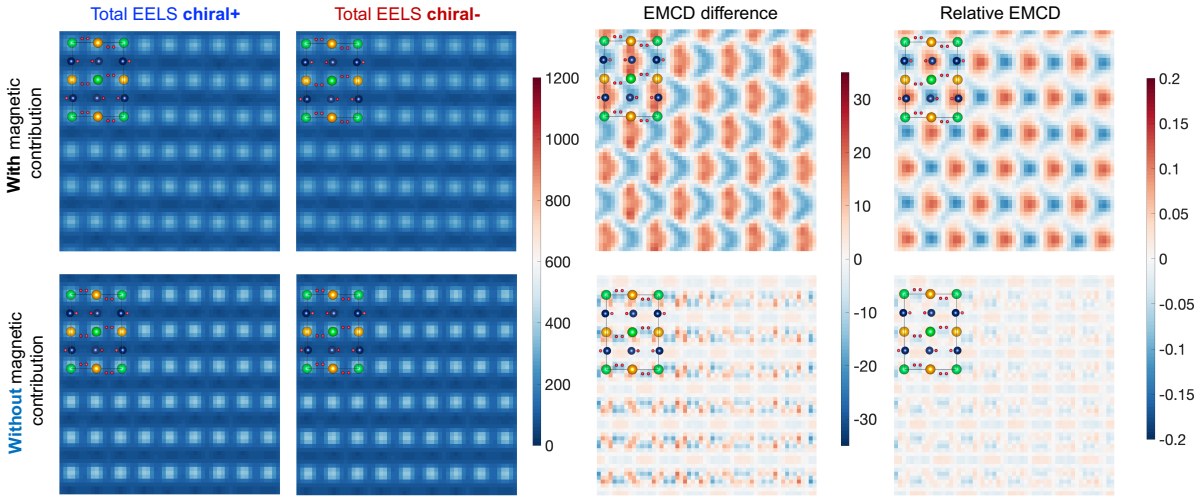


Fig. S8 | Simulation test of the effect of a half–unit-cell offset shift on EMCD signal extraction. Simulated total EELS signal maps for the *chiral+* and *chiral-* (shifted by half a unit cell with respect to *chiral+*) are shown in the left two columns. The corresponding EMCD difference and relative EMCD maps are shown in the right two columns. Upper panels: results obtained with the magnetic contribution, in which the EMCD maps preserve clear atomic magnetic contrast and reproduce the expected antiferromagnetic ordering pattern. Lower panels: results obtained without the magnetic contribution, showing very weak residual signals arising from minor misalignment between the two artificially-shifted stacks. The weak signals are localized at the Fe atomic columns (atomic model overlaid) and are clearly distinguishable from the alternating contrast characteristic of antiferromagnetic order.

Supplementary Note 9: Alternative approach for the extraction of EMCD signals at the $SmFeO_3$-$DyScO_3$ interface

This alternative approach, which is described in the Methods section, is used to extract EMCD signals at the $SmFeO_3$–$DyScO_3$ interface. It avoids subtracting two chiral EELS stacks shifted by half a unit cell. The extracted EMCD maps, which are displayed in **Fig. S9**, are consistent with the results shown in Fig. 4 of the main text, which used a half-unit-cell shift.

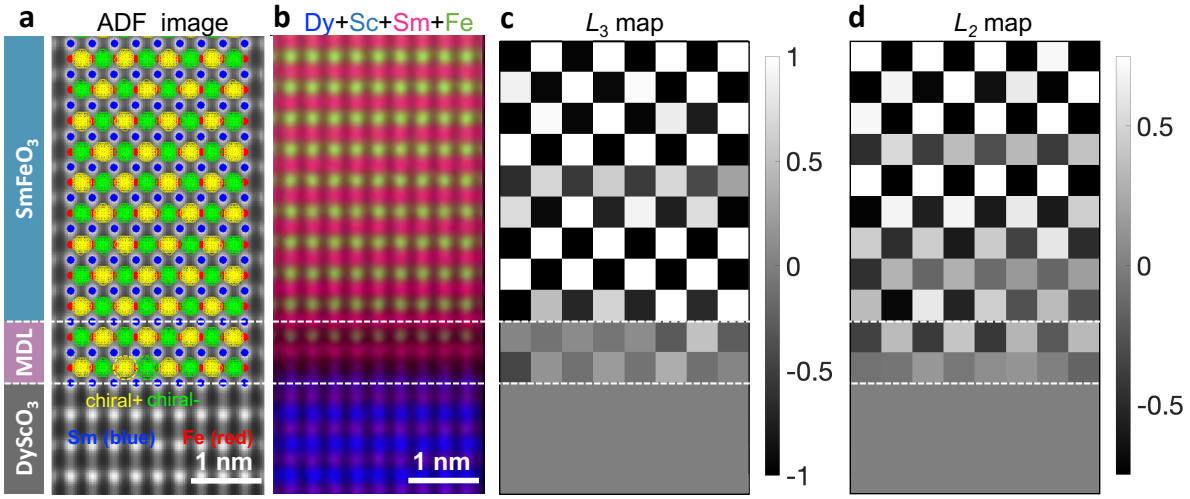


Fig. S9 | Extraction of EMCD signals at the $SmFeO_3$-$DyScO_3$ interface without applying the half-unit-cell shift described in Extended Data Fig. 5. a, ADF image across the interface after template matching. Sm (blue) and Fe (red) atomic columns are marked using corresponding colored dots. The chiral+ and chiral- regions used for chiral EELS signal extraction are indicated by yellow and green circles, respectively. **b,** Combined elemental maps for Dy (blue), Sc (violet), Sm (pink) and Fe (green) across the interface. **c,d,** EMCD maps at the L_3 and L_2 edges obtained by comparing the chiral EELS signals with the mean Fe *L*-edge spectrum.

References

1. Song, D. & Dunin-Borkowski, R. E. Three-Dimensional Measurement of Magnetic Moment Vectors Using Electron Magnetic Chiral Dichroism at Atomic Scale. *Phys. Rev. Lett.* **127**, 087202 (2021).
2. Song, D. *et al.* An in-plane magnetic chiral dichroism approach for measurement of intrinsic magnetic signals using transmitted electrons. *Nat Commun* **8**, 15348 (2017).
3. Rusz, J., Rubino, S., Eriksson, O., Oppeneer, P. M. & Leifer, K. Local electronic structure information contained in energy-filtered diffraction patterns. *Phys. Rev. B* **84**, 064444 (2011).
4. Cui, J., Sha, H., Yang, W. & Yu, R. Antiferromagnetic imaging via ptychographic phase retrieval. *Science Bulletin* **69**, 466–472 (2024).

EMCD signal remains stable for sample thicknesses below 40 nm and for convergence semi-angles of between 10 and 25 mrad, offering feasibility for experiments.

A STEM-EELS datacube was recorded experimentally from a $DyFeO_3$ crystal with a pixel size of approximately 0.3 Å. Details of the setup and parameters are provided in the Methods section and Extended Data Fig. 3. In order to enhance the SNR, a template matching method was applied[22,23] (Methods). Elemental maps were calculated by integrating the EELS signals at the Dy $M_{5,4}$, Fe $L_{3,2}$ and O K edges, as shown in Fig. 2c. The composite image reveals the atomic column positions and species. To visualize the EMCD signal, the EELS signals were first summed at all of the chiral+ and chiral- positions (indicated in Fig. 2b). The procedure is outlined in Extended Data Fig. 4. The summed chiral+ and chiral- EELS signals, as well as the resulting EMCD signals obtained by calculating their difference, are shown in Fig. 2d. Noticeable contrast of opposite sign is visible at the L_3 and L_2 edges, demonstrating the feasibility of measuring EMCD at the atomic scale for antiferromagnets that have zero net magnetization. The ratio of orbital to spin magnetic moment was calculated by applying sum rules[7,8] to the EMCD signals shown in Fig. 2d, yielding a value of 0.01 ± 0.01. This negligible value indicates that the orbital magnetic moment is quenched for Fe^{3+} ions occupying the octahedral crystal field in $DyFeO_3$ and is consistent with the results of density functional theory calculations[24].

Real-space EMCD maps for the L_3 and L_2 edges are shown in Fig. 2e-f. To generate these maps, chiral+ and chiral- signals were separated from defined regions and averaged to improve the SNR. Following background removal and post-edge normalization of the chiral EELS data, the EMCD signal was obtained through subtraction, and the EMCD maps were generated by integrating the differential signal at the respective L_3 and L_2 edges. Details of data processing are given in Extended Data Fig. 5. The alternating L_3 and L_2 patterns in the real-space maps are associated with antiferromagnetic ordering and are consistent with the simulations shown in

Fig. 2b. Furthermore, the EMCD signals from individual atomic columns were extracted along the horizontal and vertical directions marked in Fig. 2e, as shown in Fig. 2g-h. The negative L_3 (L_2) and positive L_2 (L_3) signals are clearly resolved for the Fe atom columns. These features demonstrate successful atomic-column imaging of antiferromagnetic ordering in $DyFeO_3$. The antiferromagnetic ordering was further verified by analyzing the atomic-column EMCD signals on the assumption that the spins were oriented along the *y* or *z* directions (Extended Data Figs. 6-7, Supplementary Notes 3-4 and Figs. S3-S4). The negligible EMCD signals in these measurements confirm that the spins are oriented along the *x* direction.

Imaging antiferromagnetic order in α-Fe_2O_3

In order to demonstrate its applicability to different antiferromagnetic structures, we applied our technique to α-Fe_2O_3 (hematite). α-Fe_2O_3 has a hexagonal crystal structure and exhibits nearly C-type antiferromagnetic ordering, with a Néel temperature of $T_N \sim 950$ K. The Fe^{3+} magnetic moments are aligned parallel within each (0001) basal plane, showing in-plane easy anisotropy in the $< 1\bar{1}00 >$ direction. The magnetic moments are antiparallel between successive (0001) planes, resulting in antiferromagnetic order. In our experiments, a thin Fe_2O_3 sample was oriented along the $[11\bar{2}0]$ zone axis with its spins aligned along $[1\bar{1}00]$ (Fig. 3a). The simulated real-space EMCD distribution reveals that the magnetic signals are localized between adjacent (0001) Fe atomic planes (Fig. 3b). To extract the EMCD signal, we separately integrated the EELS signals in alternating chiral+ and chiral- regions (marked in Fig. 3b) between the Fe atomic planes and calculated their difference. Data were processed using the procedure described for $DyFeO_3$. An ADF image and corresponding elemental map reveal the atomic structure and elemental distribution (Fig. 3c-d). Summed EELS signals from the chiral+ and chiral- regions yield distinct EMCD signals (Fig. 3e), confirming the feasibility of atomic column EMCD for C-type antiferromagnets. The integrated EMCD signals at the L_3 and L_2

edges reveal the expected antiferromagnetic contrast (Fig. 3f-g), consistent with the simulated results (Fig. 3b). A line profile of the EMCD intensity across the (0001) planes (Fig. 3h**)**, shows alternating signal polarity, consistent with antiferromagnetic coupling.

Magnetic dead layer at the $DyScO_3$-$SmFeO_3$ interface

Magnetic dead layers (MDLs)—regions where magnetic order is significantly suppressed—often form at interfaces between magnetic materials and adjacent substrates or capping layers, critically influencing spintronic device performance and fundamental magnetic interactions. However, directly probing these interfacial MDLs at the atomic scale remains challenging due to the limited spatial resolution of conventional magnetic characterization techniques. Here, we apply atomic-column-resolved EMCD to map the magnetism across the interface between $DyScO_3$ and the antiferromagnetic $SmFeO_3$ (Fig. 4a, Methods and Extended Data Fig. 8 for film growth and structural characterization). The small lattice mismatch between $DyScO_3$ and $SmFeO_3$ leads to a fully coherent interface (Fig. 4b).

$SmFeO_3$ has an orthorhombic crystal structure with a Néel temperature around 640 K. The Fe^{3+} ions exhibit G-type antiferromagnetic ordering with spins oriented along the *y*-axis[25], while the Sm^{3+} ions are non-magnetic at room temperature (Fig. 4a). This contrasts with the *x*-axis spin orientation in $DyFeO_3$ (Fig. 2a). In this case, the EMCD signals are distributed between adjacent Fe columns, as demonstrated in simulations (Extended Data Fig. 6). Elemental and EMCD signals mappings are shown in Fig. 4c-d, and corresponding line profiles across the interface are presented in Fig. 4e-f. The localized EMCD signals between adjacent Fe columns in Fig. 4d confirms that the spins are oriented along *y*-axis in $SmFeO_3$. The column-by-column EMCD spectra are shown in Supplementary Note 5 and Fig. S5. These results unambiguously reveal a magnetically suppressed interfacial region with a thickness of one unit cell, while the antiferromagnetic coupling is preserved (Fig. 4d). The fully strained nature of the thin film

allows us to conclusively attribute this magnetic suppression to interfacial interdiffusion, as evidenced by the chemically intermixed region (pink areas in Fig. 4e) with a composition describable as $(Sm_{1-x}Dy_x)(Fe_{1-y}Sc_y)O_3$. While previous studies proposed various mechanisms for MDL formation, including interfacial diffusion, strain effects and emergent magnetic coupling[26], our direct measurements provide definitive evidence that chemical interdiffusion plays the dominant role in this system.

The measurement of antiferromagnetic ordering across the interface benefits from atomic-column lateral resolution. With a minimum Fe–Fe atomic column spacing of approximately 2.65 Å in the present system, our method is also well suited for probing magnetic variations at other defects, such as twin boundaries, stacking faults, and, in principle, dislocations or point defects, provided that the atomic arrangement is well-defined and the sample can tolerate the required electron dose (see Supplementary Note 6 and Fig. S6). By comparison, atomic-column–resolved DPC imaging typically relies on spatial averaging over several neighboring unit cells to reconstruct local magnetic fields[5], which restricts its applicability to nearly perfect crystalline regions. Similarly, while electron holography[4] and conventional EMCD[10–12] can achieve atomic-plane resolution, they lack atomic-column lateral resolution and are intrinsically insensitive to G-type antiferromagnetic order due to the zero net magnetization per atomic plane.

Conclusions

We establish an atomic-column-resolved EMCD method for element-specific mapping of magnetic order in antiferromagnets at the atomic scale. The combined *zone-axis* diffraction geometry and *on-axis* experimetal setup make it broadly accessible in a standard aberrated-corrected TEM with EELS. This capability is demonstrated not only by resolving G-type and

C-type antiferromagnetic orders in $DyFeO_3$ and α-Fe_2O_3 crystals, but also by probing defective regions through mapping a magnetic dead layer at the buried $DyScO_3$–$SmFeO_3$ interface. This technique can be used for studying antiferromagnetism and interfacial magnetism, and is readily extendable to emerging phenomena such as altermagnets[27] and topological magnetism[28]. It also offers the potential to link magnetism with atomic and electronic structure, in particular at domain walls and interfaces that exhibit exchange bias or emergent magnetism. In the future, the use of a magnetic-field-free environment in the TEM[4,5,29] can be used to preserve intrinsic magnetic configurations, offering advantages for performing atomic-resolution magnetic studies of ferromagnets and other materials that may be affected by external magnetic fields.

Acknowledgments

The authors are grateful for financial support from the National Key R&D Program of China (No. 2022YFA1403603) (D.S. and H.D.), the National Natural Science Foundation of China (Nos. 52173215 (D.S.), 52473226 (D.S.), 12241406 (H.D.) and 52325105 (H.D.)), the National Natural Science Fund for Excellent Young Scientists Fund Program (Overseas, 2021) (D.S.), the CAS Project for Young Scientists in Basic Research (YSBR-084) (H.D.), the Strategic Priority Research Program of the Chinese Academy of Sciences (XDB33030100) (H.D.), the Chinese Academy of Sciences under contract No. JZHKYPT-2021-08 (H.D.). F.Z. acknowledges financial support from the Fundamental Research Funds for the Central Universities and the National Natural Science Fund for Excellent Young Scientists Fund Program (Overseas). R.E.D.-B. is grateful for financial support from the European Research Council under the European Union's Horizon 2020 Research and Innovation Programme (Grant No. 856538, project "3D MAGiC") and the Deutsche Forschungsgemeinschaft (project ID 405553726; TRR 270). This work made use of the resources of the Center for Electron Microscopy at Anhui University and the Ernst Ruska-Centre for Microscopy and Spectroscopy

265 with Electrons at Forschungszentrum Jülich. D.S. thank Jan Rusz for providing MATS v2
266 software and helpful discussion.
267

268 **Author contributions**

269 D.S., H.D. and R.E.D.-B. supervised the study. D.S. conceived the idea and initiated the study.
270 D.S. conducted the EMCD simulations, experiments and analyzed the data. H.D. prepared the
271 TEM sample. L.H. prepared the $SmFeO_3$ thin films. L.J. performed NanoMill experiments.
272 Y.K. synthesized the $DyFeO_3$ crystal. B.G. and M.T. provided support for the facilities. D.S.
273 and F.Z. wrote the manuscript with input from H.D., Y.L. and R.E.D.-B. All of the authors
274 discussed the results and contributed to the manuscript.
275

276 **Competing interests**

277 The authors declare no competing interests.
278

Figure captions

Fig. 1 | Principle of atomic-column EMCD imaging *via* STEM-EELS using transmitted electrons. a, Schematic of the STEM-EELS setup for antiferromagnet $DyFeO_3$ with a G-type spin configuration. The electron beam propagates along the z-axis. The Néel vector is oriented along the *x*-axis. An annular dark-field (ADF) detector captures an atomic-resolution image simultaneously with EELS acquisition. The diffraction pattern contains both nonmagnetic and magnetic contributions. A post-column spectrometer records the EELS signals on a digital detector. **b,** Atomic model of $DyFeO_3$ projected along the *z*-axis. Fe atoms (green and orange) have spin orientations along $\pm x$. Stars mark three real-space electron probe positions. **c-e,** Simulated nonmagnetic (**c**), magnetic (**d**) and total (**e**) signals in the diffraction plane at an energy loss of 710 eV for the three probe positions defined in **b**. The semi-convergence angle is 17.8 mrad and the sample thickness is 22.38 nm. Dashed circles denote the *on-axis* EELS entrance aperture. The diffraction plane extends over $q_x = \pm 40$ mrad and $q_y = \pm 40$ mrad. The integrated nonmagnetic signal from the *on-axis* EELS aperture is identical for the two chiral positions (black and red stars), whereas the integrated magnetic signals are opposite in sign, giving rise to position-dependent chiral EELS signals. **f,** Schematic illustration of the total chiral EELS signals in **e** from two chiral probe positions described in **b**, shown for the Fe $L_{3,2}$ edges. Their difference yields the EMCD signal for a single atomic column. **g,** 3D datacube obtained from the STEM-EELS experiment, with *x* and *y* representing the real-space scanning dimensions.

Fig. 2 | Atomic-column-resolved EMCD signals in the G-type antiferromagnet $DyFeO_3$. **a,** Atomic model of $DyFeO_3$ projected along the *z*-axis, showing the spin orientations of the Fe atoms. **b,** Simulated real-space magnetic EMCD signals for the region shown in **a**. The Fe atomic model is overlaid to highlight the EMCD signal distribution, with chiral+ and chiral− positions indicated. **c,** ADF image and elemental maps of Dy, Fe and O calculated from a STEM-EELS datacube after template-matching processing. The rightmost panel shows a combined elemental map. **d,** Averaged chiral EELS and EMCD signals obtained from the chiral+ and chiral− positions across the entire STEM-EELS datacube. **e,f,** L_3 and L_2 EMCD maps generated by integrating the EMCD signals at the $L_{3,2}$ edges. **g,h**, EMCD signals for individual atomic columns in the horizontal and vertical directions, corresponding to the dashed rectangles in **e**. **c**, **e** and **f** have the same image size and the scale bar is 5 Å.

Fig. 3 | Atomic-resolution EMCD signals in hematite (α-Fe_2O_3). **a,** Atomic model of α-Fe_2O_3 projected along the $[11\bar{2}0]$ direction, with the spin orientations of Fe atoms aligned along $[1\bar{1}00]$ within the *ab*-plane. **b,** Simulated real-space EMCD signal distribution for the region shown in **a**. The chiral+ and chiral- regions are indicated. **c,** ADF image obtained after template matching processing. **d,** Combined elemental maps of Fe and O. **e,** Averaged chiral EELS and corresponding EMCD signals extracted from the chiral+ and chiral− regions across the entire STEM-EELS datacube. **f,g,** EMCD maps generated by integrating the EMCD signals at the L_3 and L_2 edges, respectively. **h,** Line profiles extracted from the L_3 and L_2 EMCD maps shown in **g** and **h**, averaged in the horizontal direction. **c**, **d**, **f** and **g** have the same image size and the scale bar is 5 Å.

Fig. 4 | Magnetic dead layer at the $DyScO_3$-$SmFeO_3$ interface. a, Atomic models of $DyScO_3$ and $SmFeO_3$ oriented along the z-axis. The spins in $SmFeO_3$ are aligned along the *y*-axis. **b,c,** ADF image and combined elemental maps of Dy (blue), Sc (violet), Sm (pink) and Fe (green) across the interface. **d,** EMCD map generated by integrating the EMCD signals at the L_3 edge. The layer and column numbers are indicated in sequence. **e,f**, Extracted profiles of elemental mapping and integrated EMCD signals for individual atomic columns across the interface. The magnetic dead layer (MDL) is marked by dashed lines and pink rectangle in **b-f**. The scale bar in **b** represents 1 nm.

References

1. van der Laan, G. *et al.* Experimental proof of magnetic x-ray dichroism. *Phys. Rev. B* **34**, 6529–6531 (1986).
2. van der Laan, G. & Figueroa, A. I. X-ray magnetic circular dichroism—A versatile tool to study magnetism. *Coord. Chem. Rev.* **277–278**, 95–129 (2014).
3. Cui, J., Sha, H., Yang, W. & Yu, R. Antiferromagnetic imaging via ptychographic phase retrieval. *Sci. Bull.* **69**, 466–472 (2024).
4. Tanigaki, T. *et al.* Electron holography observation of individual ferrimagnetic lattice planes. *Nature* **631**, 521–525 (2024).
5. Kohno, Y., Seki, T., Findlay, S. D., Ikuhara, Y. & Shibata, N. Real-space visualization of intrinsic magnetic fields of an antiferromagnet. *Nature* **602**, 234–239 (2022).
6. Schattschneider, P. *et al.* Detection of magnetic circular dichroism using a transmission electron microscope. *Nature* **441**, 486–488 (2006).
7. Rusz, J., Eriksson, O., Novák, P. & Oppeneer, P. M. Sum rules for electron energy loss near edge spectra. *Phys. Rev. B* **76**, 060408 (2007).
8. Calmels, L. *et al.* Experimental application of sum rules for electron energy loss magnetic chiral dichroism. *Phys. Rev. B* **76**, 060409 (2007).
9. Ali, H. *et al.* Noise-dependent bias in quantitative STEM-EMCD experiments revealed by bootstrapping. *Ultramicroscopy* **257**, 113891 (2024).
10. Rusz, J. *et al.* Magnetic measurements with atomic-plane resolution. *Nat. Commun.* **7**, 1–7 (2016).
11. Wang, Z. *et al.* Atomic scale imaging of magnetic circular dichroism by achromatic electron microscopy. *Nat. Mater.* **17**, 221–225 (2018).
12. Ali, H. *et al.* Visualizing subatomic orbital and spin moments using a scanning transmission electron microscope. *Nat. Mater.* **24**, 1215–1220 (2025).

13. Kimoto, K. *et al.* Element-selective imaging of atomic columns in a crystal using STEM and EELS. *Nature* **450**, 702–704 (2007).
14. Muller, D. A. *et al.* Atomic-Scale Chemical Imaging of Composition and Bonding by Aberration-Corrected Microscopy. *Science* **319**, 1073–1076 (2008).
15. Idrobo, J. C. *et al.* Detecting magnetic ordering with atomic size electron probes. *Adv. Struct. Chem. Imaging* **2**, 1–10 (2016).
16. Rusz, J., Rubino, S. & Schattschneider, P. First-principles theory of chiral dichroism in electron microscopy applied to 3d ferromagnets. *Phys. Rev. B* **75**, 214425 (2007).
17. Calmels, L. & Rusz, J. Momentum-resolved EELS and EMCD spectra from the atomic multiplet theory: Application to magnetite. *Ultramicroscopy* **110**, 1042–1045 (2010).
18. Song, D. & Dunin-Borkowski, R. E. Three-Dimensional Measurement of Magnetic Moment Vectors Using Electron Magnetic Chiral Dichroism at Atomic Scale. *Phys. Rev. Lett.* **127**, 087202 (2021).
19. Ritter, C. *et al.* The magnetic structure of $DyFeO_3$ revisited: Fe spin reorientation and Dy incommensurate magnetic order. *J. Phys. Condens. Matter* **34**, 265801 (2022).
20. Song, D. *et al.* An in-plane magnetic chiral dichroism approach for measurement of intrinsic magnetic signals using transmitted electrons. *Nat. Commun.* **8**, 15348 (2017).
21. Rusz, J. *et al.* Localization of magnetic circular dichroic spectra in transmission electron microscopy experiments with atomic plane resolution. *Phys. Rev. B* **95**, 174412 (2017).
22. Jones, L. *et al.* Managing dose-, damage- and data-rates in multi-frame spectrum-imaging. *Microscopy* **67**, i98–i113 (2018).
23. Haruta, M. *et al.* Atomic-resolution two-dimensional mapping of holes in the cuprate superconductor $La_{2-x}Sr_xCuO_{4\pm\delta}$. *Phys. Rev. B* **97**, 205139 (2018).
24. Cui, R. *et al.* Role of Dy 4f electrons on magnetic coupling and reorientation in $DyFeO_3$. *J. Phys. Condens. Matter* **36**, 335501 (2024).

25. Kuo, C.-Y. *et al.* k=0 Magnetic Structure and Absence of Ferroelectricity in SmFeO3. *Phys. Rev. Lett.* **113**, 217203 (2014).
26. Luo, W. Magnetic "Dead" Layer at a Complex Oxide Interface. *Phys. Rev. Lett.* **101**, (2008).
27. Šmejkal, L., Sinova, J. & Jungwirth, T. Emerging Research Landscape of Altermagnetism. *Phys. Rev. X* **12**, 040501 (2022).
28. Bernevig, B. A., Felser, C. & Beidenkopf, H. Progress and prospects in magnetic topological materials. *Nature* **603**, 41–51 (2022).
29. Shibata, N. *et al.* Atomic resolution electron microscopy in a magnetic field free environment. *Nat. Commun.* **10**, 2308 (2019).

Methods

Sample preparation

A $DyFeO_3$ single crystal was grown using a floating zone method[30]. [0001]-oriented **α**-Fe_2O_3 single crystal was purchased from MTI Corporation. Epitaxial thin film of $SmFeO_3$ were grown on $DyScO_3$ (001) substrate using the pulsed laser deposition (PLD) technique. The substrate temperature and oxygen pressure during deposition were set to 850 °C and 0.05 mbar, respectively. PLD was performed with a KrF excimer UV laser (λ = 248 nm), using an energy density of 1.5 J/cm² and a repetition rate of 2 Hz. After deposition, the films were cooled to room temperature at a rate of 10 °C/min under an oxygen partial pressure of approximately 0.5 bar. For TEM and EMCD experiments, the samples were initially thinned to electron transparency by using a focused ion beam (FIB) system (Helios NanoLab 600i; FEI) equipped with an Omniprobe 200+ micromanipulator at 30 kV. The amorphous layer on the sample surface was removed at 2 kV. The FIB lamellae were further processed with Ar ions at 3 kV on a Bal-Tec RES 101 ion beam milling system and at 900 V and 500 V on a Fischione Nanomill 1040 system, in order to thin them further and to eliminate surface damage.

EMCD simulations

EMCD simulations were performed using MATS v2 software, which employs a combined multislice and Bloch-wave method and was developed by Jan Rusz[31,32]. Chiral EELS signals in the diffraction plane, which are evaluated based on a double-differential scattering cross-section (DDSCS) for momentum-resolved inelastic electron scattering, can be expressed as a linear superposition of nonmagnetic and magnetic EMCD contributions within the dipole approximation:

$$\frac{\partial^2\sigma}{\partial E\partial\Omega} \propto A * N(E) + B * M(E)$$

where $N(E)$ and $M(E)$ are the nonmagnetic and magnetic EMCD signals, respectively. For nonmagnetic materials, M(E) is zero. The coefficients A and B represent the intensities of the nonmagnetic and magnetic EMCD signals, respectively. They are determined from the product of Bloch coefficients and momentum transfers[32] and are influenced by experimental parameters, including the crystal structure, sample thickness and imaging conditions. The relative intensity of the EMCD signal is defined as the ratio B/A. Magnetic signals from the three Cartesian directions can be calculated separately by modifying the momentum transfer terms.

In the simulations, orthogonal supercell of $DyFeO_3$, **α-**Fe_2O_3 and $SmFeO_3$ was constructed and oriented along desired directions, with the electron beam parallel to the z axis. All aberrations were set to zero. The accelerating voltage, beam position, convergence semi-angle and sample thickness were adjusted as required. An energy loss of 710 eV, corresponding to the Fe L_3 edge, was used to calculate energy-selected diffraction patterns. At a fixed electron beam position, the distributions of the nonmagnetic and magnetic EMCD signals were computed for each pixel in the diffraction plane. The diffraction pattern range was set to ±40 mrad in the q_x and q_y directions with a step size of 2.5 mrad, as shown in Fig. 1c-e, Fig. 2b, Fig. 3b and Extended Data Fig. 1. Note that in antiferromagnetic $DyFeO_3$, the Fe atoms form two magnetic sublattices with opposite spin orientations. In our simulations, we explicitly separate the nonmagnetic and magnetic contributions from each sublattice. The final EMCD signal is obtained by taking the difference between their respective magnetic contributions. The details are presented in Supplementary Note 2 and Fig. S2.

STEM experiments

The atomic structure of the crystals was imaged using high-angle annular dark-field scanning transmission electron microscopy (HAADF-STEM) and integrated differential phase contrast scanning transmission electron microscopy (iDPC-STEM), as shown in Extended Data Fig. 8.

Experiments were conducted on a Thermo Fisher Scientific Titan Themis Z microscope operated at 300 kV. This microscope is equipped with a probe corrector, a four-segment DF4 detector and a Gatan GIF Continuum K3 dual-EELS system. The convergence semi-angle for STEM imaging was set to 25 mrad, with collection semi-angles of 50-200 mrad for HAADF imaging and 8-42 mrad for iDPC imaging. The beam current was 30 pA. iDPC images were reconstructed from four-segment images, making use of a high-pass filter to eliminate low frequency information. Data acquisition and processing were performed using commercial Velox software. The sample thickness was measured using position-averaged convergent beam electron diffraction (PACBED), as shown in Extended Data Fig. 3. The convergence semi-angle for PACBED was approximately 6.75 mrad and PACBED patterns were recorded using the K3 camera. PACBED simulations were performed using Dr. Probe software[33] for the same parameters as those used in the experiments.

Atomic-column EMCD experiments

Atomic-column EMCD experiments used the same experimental setup as for conventional atomic-column STEM-EELS, employing an *on-axis* EELS entrance aperture and requiring no additional facilities or modifications. The convergence semi-angle was optimized to be ~17.8 mrad. The collection semi-angle was calibrated to be ~40 mrad. EELS signals were recorded using a K3 camera installed on the post-column Gatan imaging filter. The beam current was set to 50-80 pA with a pixel dwell time of 2-3 ms, as a result of its resistance to irradiation damage. The pixel size was 0.325 Å and the EELS energy dispersion was set to 0.35 eV per channel.

The primary difference between this setup and that used for conventional EMCD results from the localization of the magnetic signals around the directly transmitted electron beam, which allows for the use of an *on-axis* aperture, and in turn offers a significantly improved signal-to-

noise ratio compared to previous *off-axis* acquisition methods (Supplementary Note 1 and Fig. S1). This concept relies on the magnetization being oriented perpendicular to the electron beam direction, facilitating the redistribution of signals in the diffraction plane[11,12]. Moreover, the zone-axis EMCD geometry is robust against beam misorientation, maintaining stable signal strength and spatial distribution for tilt variations up to 5 mrad in $DyFeO_3$ (Supplementary Note 7 and Fig. S7). This tolerance is significantly broader than that of conventional three-beam configuration[11,12], which typically requires sub-milliradian alignment to preserve signal integrity.

Extraction of atomic-column-by-atomic-column EMCD signals

Atomic-column EMCD signals were extracted from the experimental STEM-EELS datacubes, in which the *x* and *y* directions correspond to the scanning regions in real space and the *z* axis represents energy loss. The STEM-EELS experiments generate three data files: an atomic-column-resolved ADF image (size: m × n), a corresponding low-loss EELS datacube (LL; size: m × n × p) and a high-loss EELS datacube (HL; size: m × n × p). Energy calibration is first performed on the HL datacube by aligning the peak of the LL datacube to zero using Digital Micrograph software. Subsequently, data processing involves: (1) Summing the EELS signals at the chiral+ and chiral- positions, as defined in Fig. 2b and Fig. 3b, to visualize the averaged EMCD signals (shown in Fig. 2d and Fig. 3e); (2) Mapping the EMCD signals in real space with atomic-column resolution (shown in Fig. 2e-f, Fig. 3f-g and Fig. 4d).

In the first case, the procedure is outlined in the form of a flowchart in Extended Data Fig. 4. The positions of the Dy and Fe atomic columns are identified and fitted based on the ADF image. For each of the defined chiral positions (chiral+ and chiral-), the EELS signals are extracted and summed. Post-processing steps, including background removal and post-edge

normalization, are applied to the two chiral EELS signals. The EMCD signal is obtained by calculating the difference between the chiral+ and chiral- signals, as shown in Fig. 2d.

In the second case, the procedure is outlined in Extended Data Fig. 5. As in the first case, the Dy and Fe atomic column positions are identified and fitted from the ADF image. Taking the position of the Dy atoms as the center, a region of interest (ROI) of size 50 × 50 pixels is extracted. The ROIs are divided into two groups: the ADF stack for chiral+ ($50 \times 50 \times N^{+}$) and the ADF stack for chiral- ($50 \times 50 \times N^{-}$). There is a half–unit-cell offset between the two chiral datasets. Note that this offset leads to mixing of inequivalent atomic sites in $DyFeO_3$, particularly the oxygen sublattices, when subtracting the two stacks to obtain the final EMCD maps. This issue arises in $DyFeO_3$ but does not occur in all systems, such as in α-Fe_2O_3 in Fig. 3. However, since the EMCD technique is element-specific, misalignment of the oxygen sublattice would not significantly influence the EMCD maps at the Fe *L* edges (see the simulation test and discussion in Supplementary Note 8 and Fig. S8), particularly after the background removal and post-edge normalization of the EELS signals at each pixel (Extended Data Fig. 5, in which the spectrum image of the Fe sublattice after background removal and post-edge normalization is nearly identical between the two datasets). Additionally, in STEM–EELS experiments with a long acquisition time, instrumental instabilities and sample drift can introduce distortions in both the ADF and the EELS stacks, leading to slight deviations from perfectly conjugate probe positions.

In order to address the potential misalignments arising from both lattice distortion and sample drift, we applied non-rigid image registration between the chiral+ and chiral- datasets. This approach ensures accurate alignment prior to subtraction, thereby minimizing residual lattice offsets and preventing potentional artificial contrast. Then, the two ADF stacks are summed to generate two ADF images. The same procedure is applied to the HL datacube, yielding two EELS datacubes (chiral+ and chiral-) with improved signal-to-noise ratio. Finally, post-

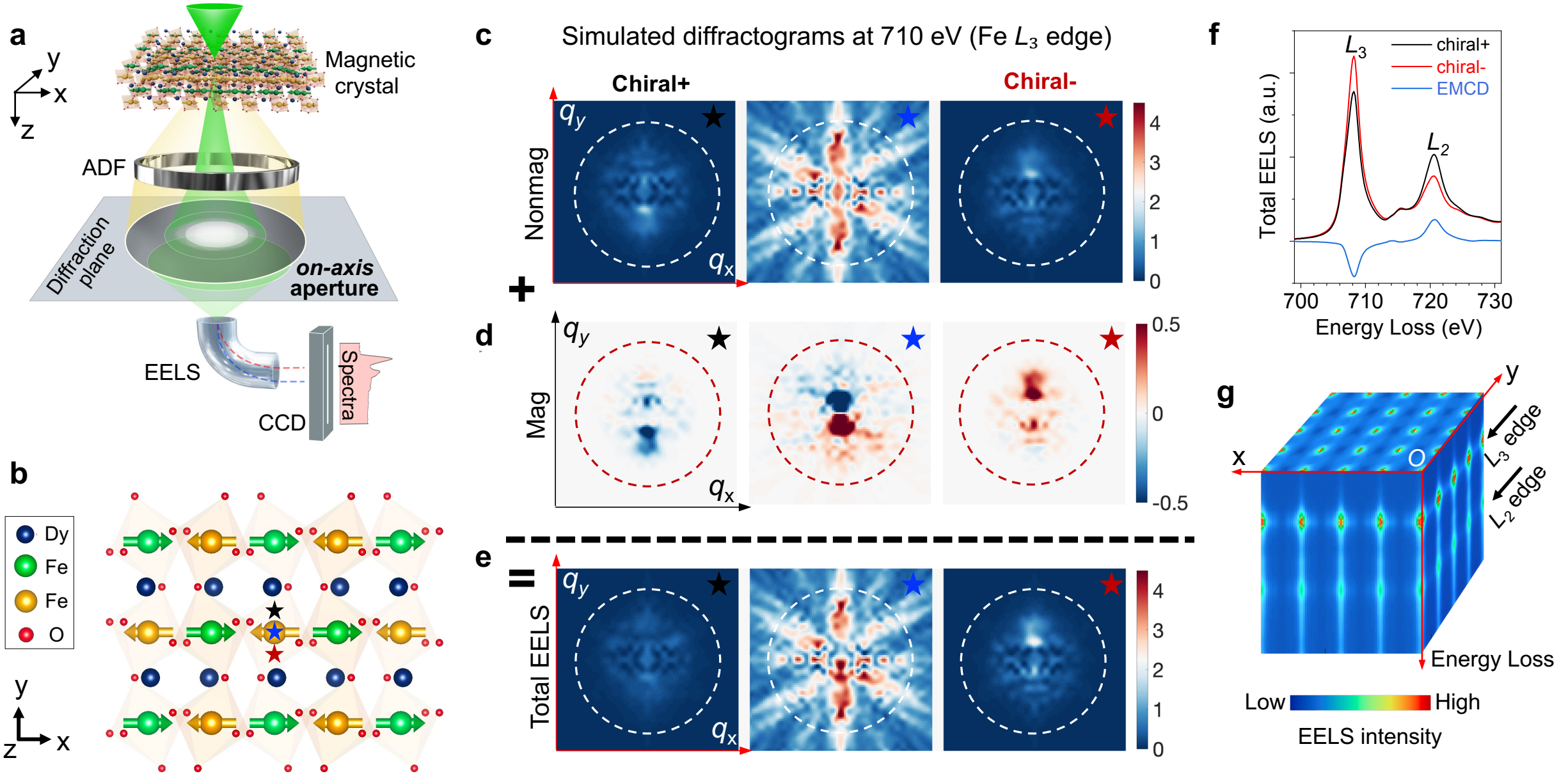
processing steps, including background removal and post-edge normalization, are applied to the two datacubes. The EMCD datacube is obtained by calculating the difference between the chiral+ and chiral- datacubes. The magnetic ordering maps shown in Fig. 2e-f were obtained by integrating the EMCD signals at the L_3 and L_2 edges. For the $DyScO_3$-$SmFeO_3$ interface, signal averaging was performed in a similar way, with data acquired by conducting multiple STEM-EELS measurements across the interface.

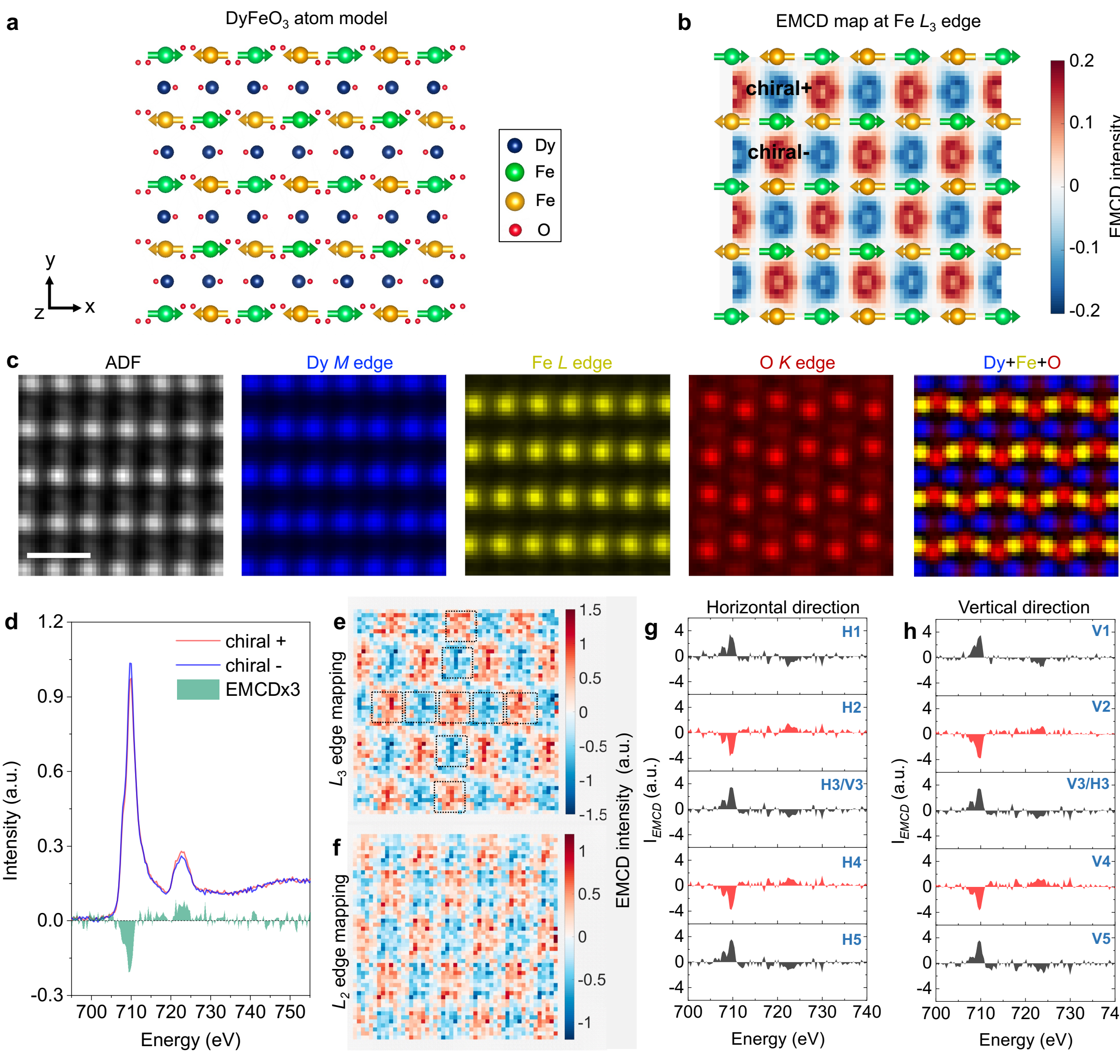
Additionally, we processed our data using the alternative approach outlined below, without applying a half-unit-cell shift described in Extended Data Fig. 5: (1) We defined the mean Fe *L*-edge spectrum (Fe_mean) as the average of the two chiral spectra shown in Extended Data Fig. 4. (2) We compared this Fe_mean spectrum with the Fe *L*-edge spectra extracted from the Dy-site regions in the spectrum images. (3) We calculated the difference between the Dy-site ROI spectra and the Fe_mean spectrum at both the L_3 and L_2 edges to generate the EMCD maps. Based on this procedure, we calculated the EMCD maps at the L_3 and L_2 edges, as shown in Extended Data Fig. 9 for $DyFeO_3$, and Supplementary Note 9 and Fig. S9 for $DyScO_3$-$SmFeO_3$ interface. The results also clearly reveal the antiferromagnetic ordering, providing complementary validation of our conclusions.

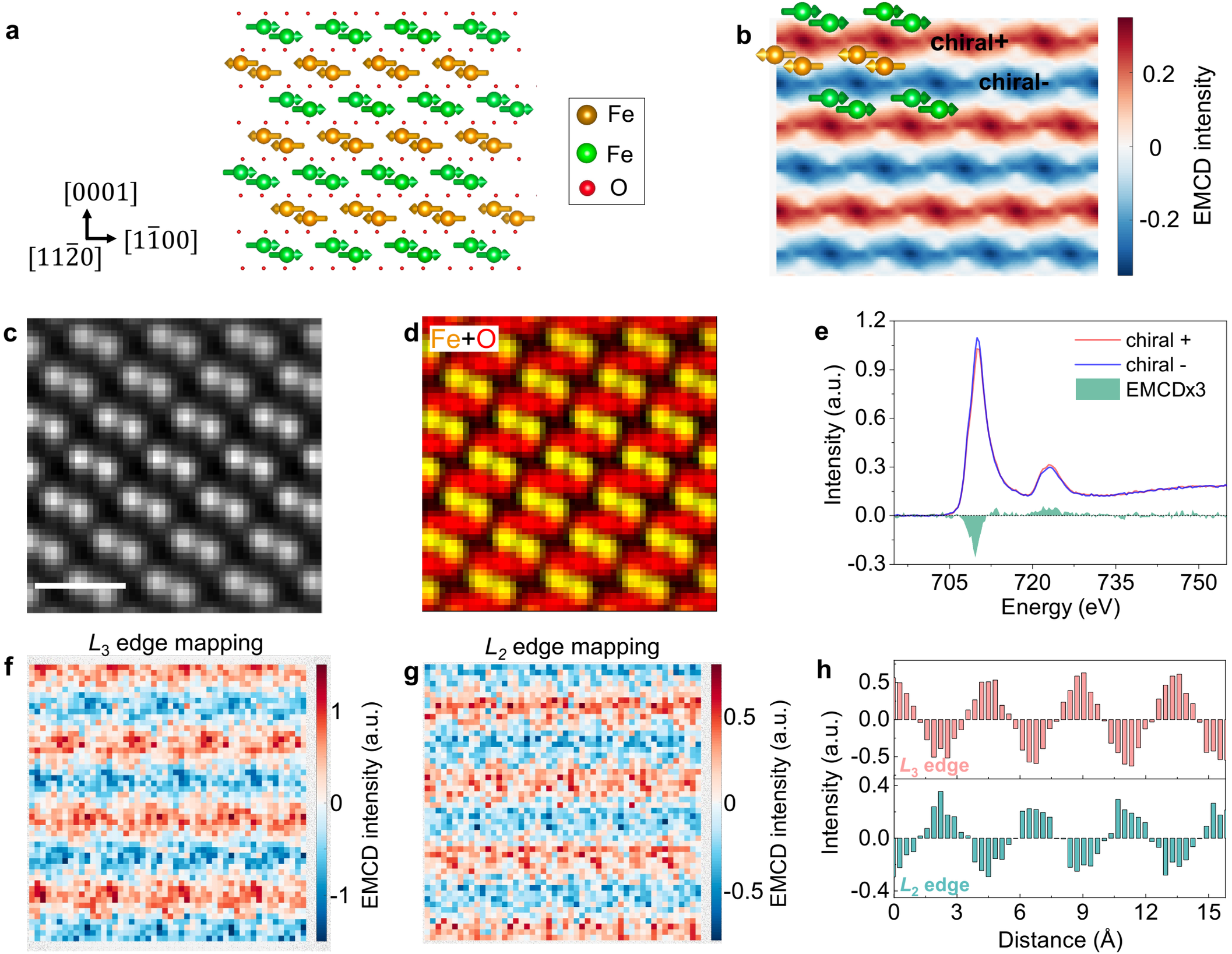
Data availability

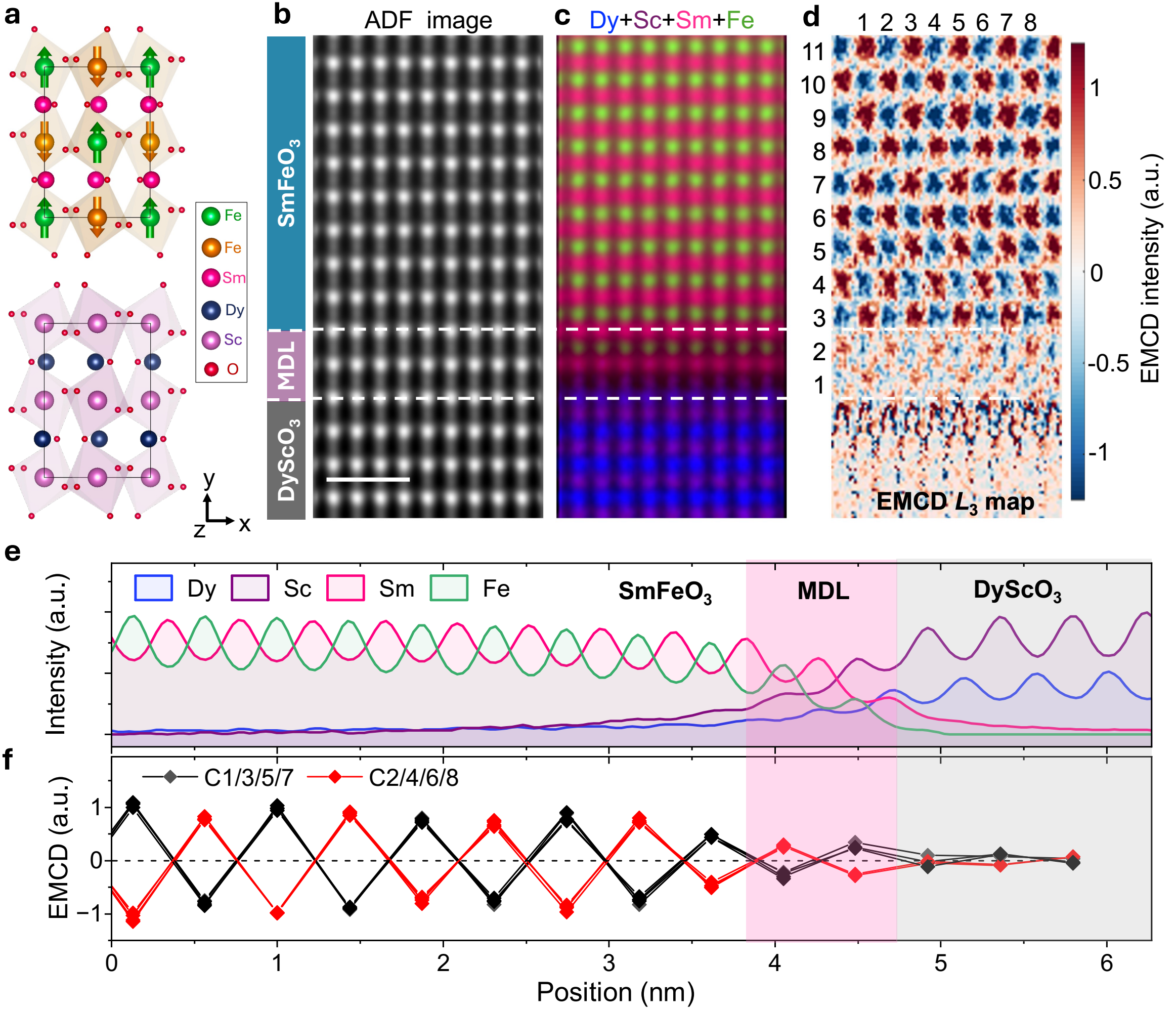
Raw experimental data and key processed results for this study are available at Zenodo: 10.5281/zenodo.18238440. All other data supporting the findings are included in the Article and its Supplementary Information. Additional information related to this work can be obtained from the corresponding authors upon reasonable request.

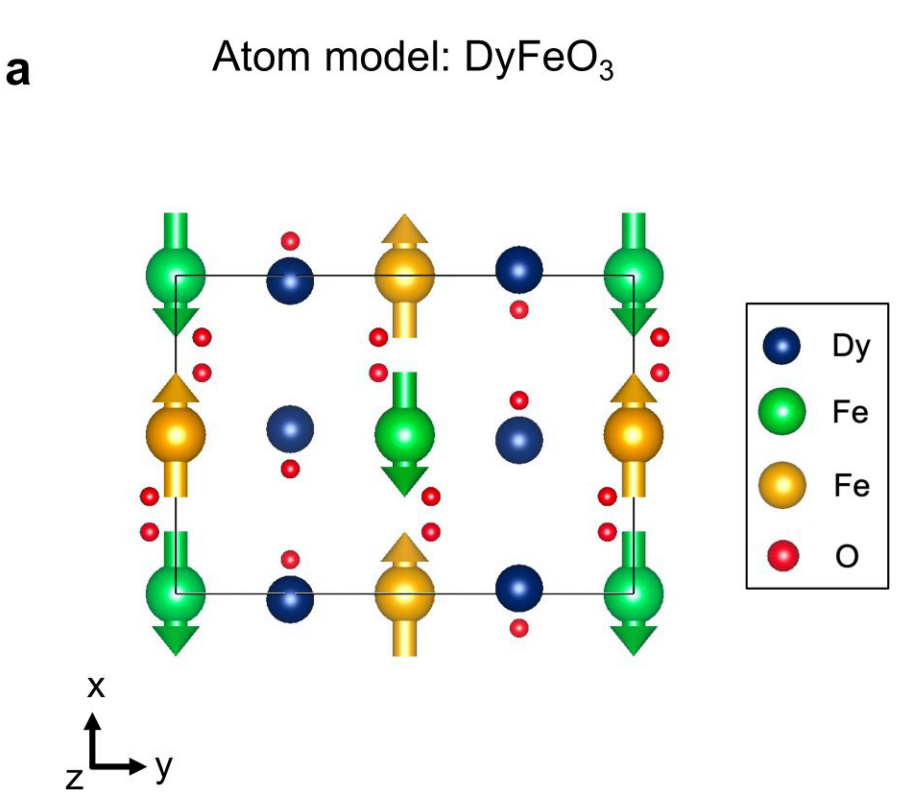
30. Ke, Y.-J., Zhang, X.-Q., Ge, H., Ma, Y. & Cheng, Z.-H. Low field induced giant anisotropic magnetocaloric effect in $DyFeO_3$ single crystal. *Chin. Phys. B* **24**, 037501 (2015).
31. Rusz, J., Bhowmick, S., Eriksson, M. & Karlsson, N. Scattering of electron vortex beams on a magnetic crystal: Towards atomic-resolution magnetic measurements. *Phys. Rev. B* **89**, 134428 (2014).
32. Rusz, J. Modified automatic term selection v2: A faster algorithm to calculate inelastic scattering cross-sections. *Ultramicroscopy* **177**, 20–25 (2017).
33. Barthel, J. Dr. Probe: A software for high-resolution STEM image simulation. *Ultramicroscopy* **193**, 1–11 (2018).

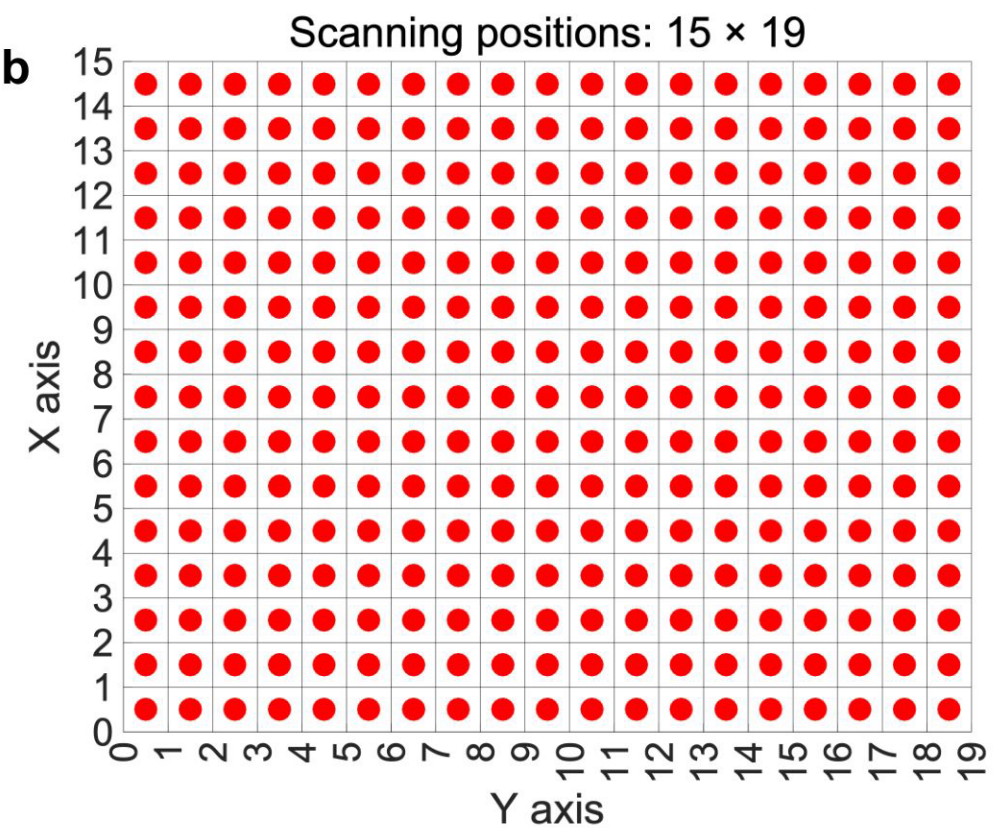

a
y
x
z
Magnetic crystal
ADF
Diffraction plane
on-axis aperture
EELS
CCD
Spectra
b
Dy
Fe
Fe
O
y
z
x
c
Simulated diffractograms at 710 eV (Fe L_3 edge)
Chiral+
Chiral-
Nonmag
q_y
q_x
4
3
2
1
0
+
d
Mag
0.5
0
-0.5
=
e
Total EELS
f
L_3
L_2
chiral+
chiral-
EMCD
Total EELS (a.u.)
700
710
720
730
Energy Loss (eV)
g
y
x
O
L_3 edge
L_2 edge
Energy Loss
Low
High
EELS intensity

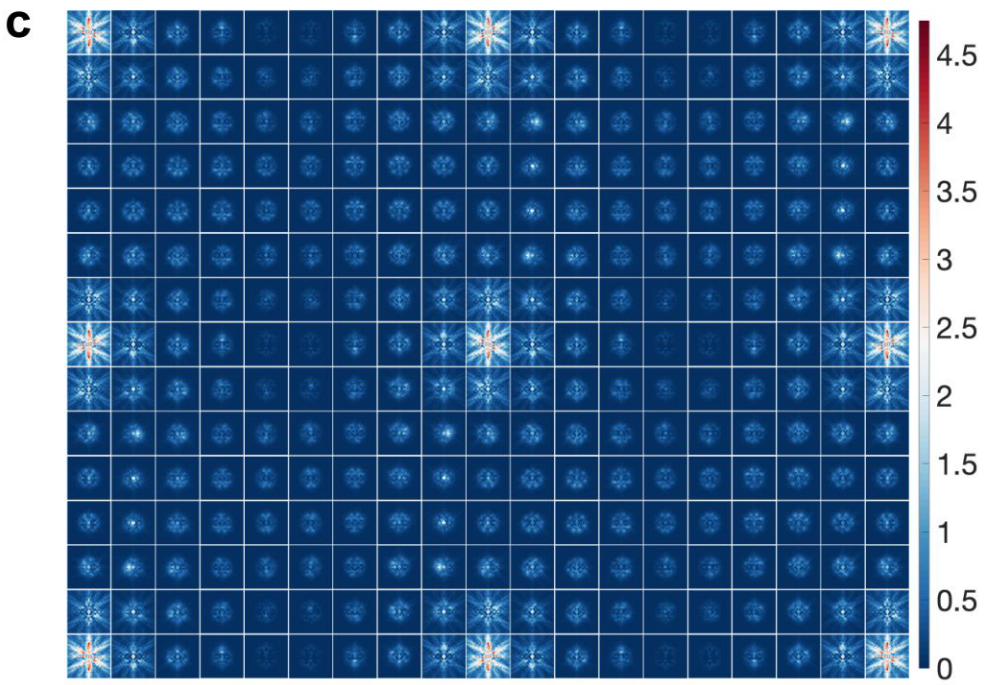

a
DyFeO3 atom model
Dy
Fe
Fe
O
y
x
z
b
EMCD map at Fe L3 edge
chiral+
chiral-
0.2
0.1
0
-0.1
-0.2
EMCD intensity
c
ADF
Dy M edge
Fe L edge
O K edge
Dy+Fe+O
d
chiral +
chiral -
EMCDx3
Intensity (a.u.)
Energy (eV)
e
L3 edge mapping
f
L2 edge mapping
EMCD intensity (a.u.)
g
Horizontal direction
H1
H2
H3/V3
H4
H5
I_EMCD (a.u.)
Energy (eV)
h
Vertical direction
V1
V2
V3/H3
V4
V5
I_EMCD (a.u.)
Energy (eV)

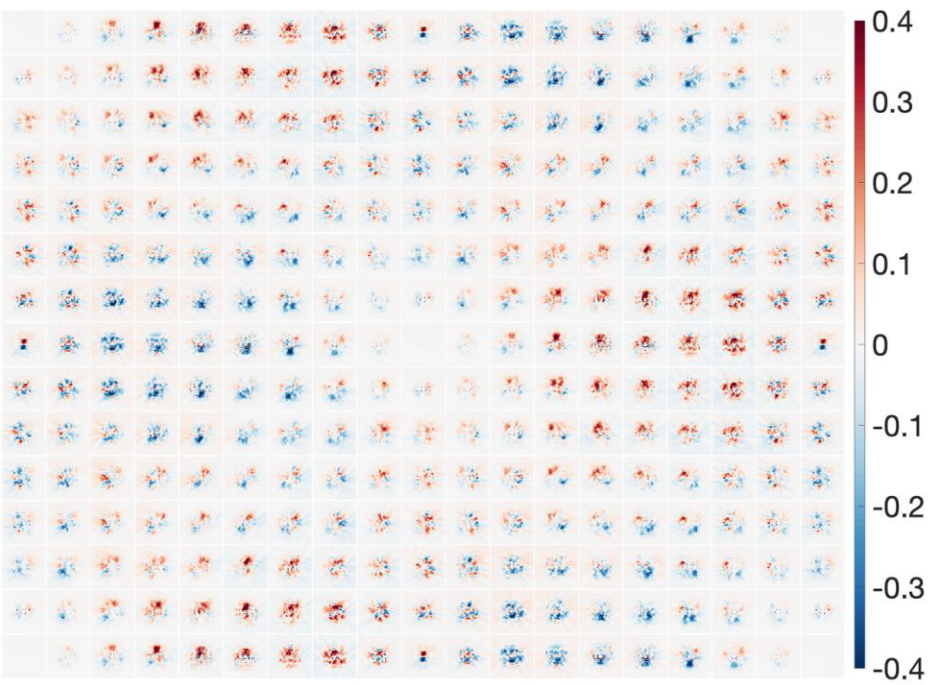

a
[0001]
[11$\bar{2}$0]
[1$\bar{1}$00]
Fe
Fe
O
b
chiral+
chiral-
0.2
0
-0.2
EMCD intensity
c
d
Fe+O
e
1.2
0.9
0.6
0.3
0.0
-0.3
Intensity (a.u.)
chiral +
chiral -
EMCDx3
705
720
735
750
Energy (eV)
f
L_3 edge mapping
1
0
-1
EMCD intensity (a.u.)
g
L_2 edge mapping
0.5
0
-0.5
EMCD intensity (a.u.)
h
0.5
0.0
-0.5
L_3 edge
0.4
0.0
-0.4
L_2 edge
Intensity (a.u.)
0
3
6
9
12
15
Distance (Å)

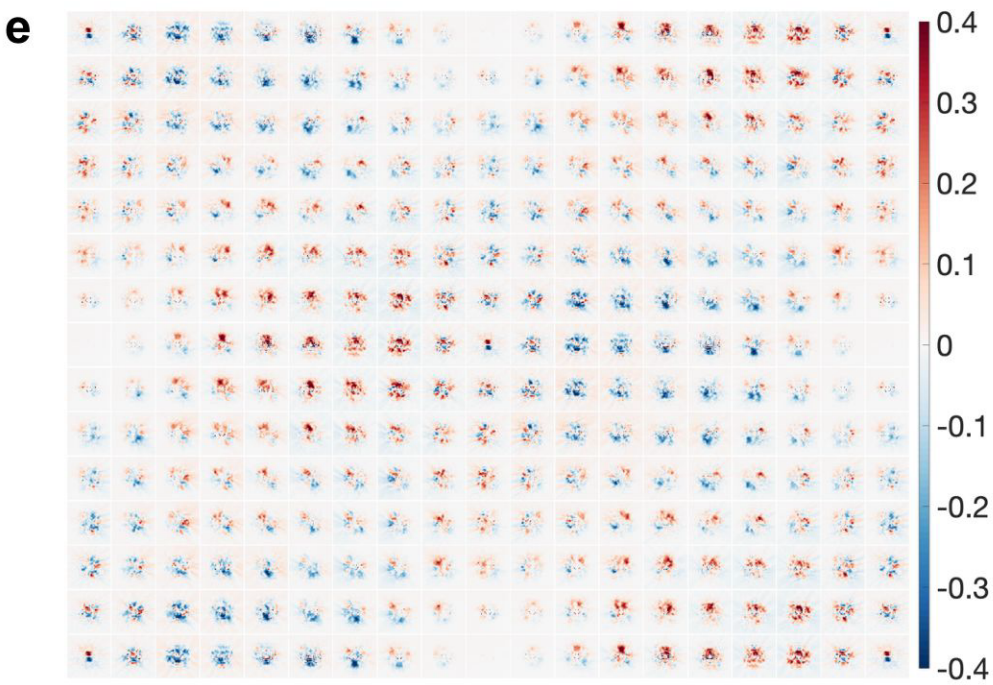

a
Fe
Fe
Sm
Dy
Sc
O
y
z
x
b
ADF image
SmFeO3
MDL
DyScO3
c
Dy+Sc+Sm+Fe
d
1 2 3 4 5 6 7 8
11
10
9
8
7
6
5
4
3
2
1
EMCD L3 map
1
0.5
0
-0.5
-1
EMCD intensity (a.u.)
e
Dy
Sc
Sm
Fe
SmFeO3
MDL
DyScO3
Intensity (a.u.)
f
C1/3/5/7
C2/4/6/8
EMCD (a.u.)
1
0
−1
0
1
2
3
4
5
6
Position (nm)

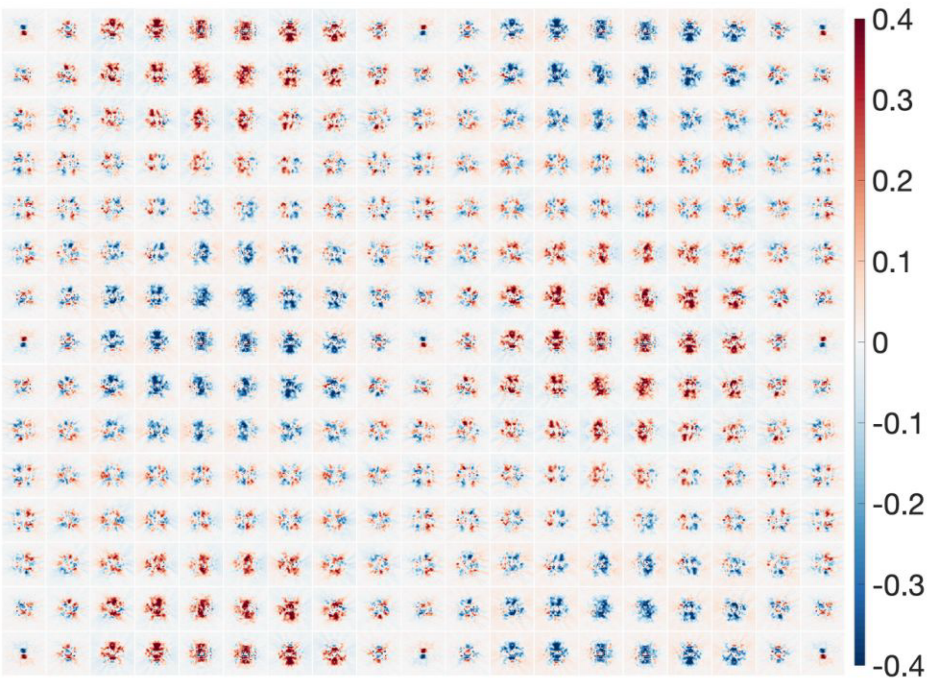

a
Atom model: $DyFeO_3$
Dy
Fe
Fe
O
x
y
z

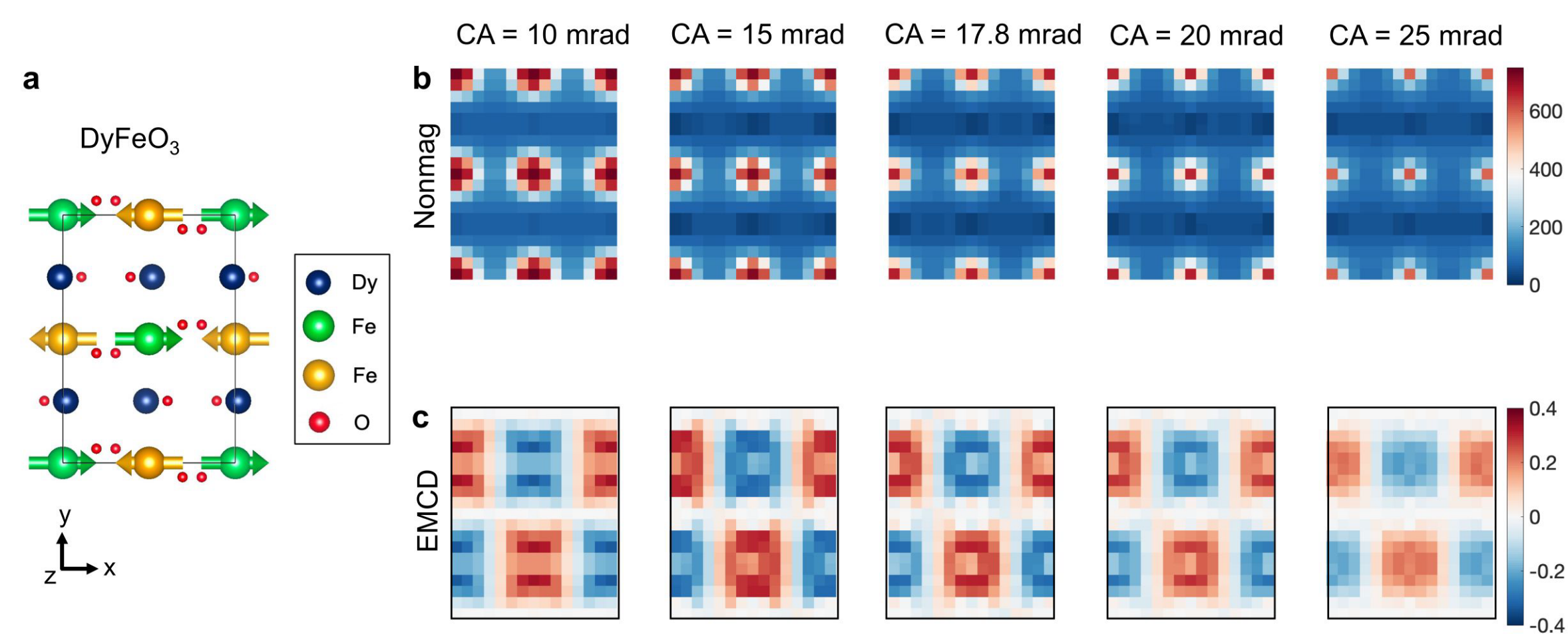

b
Scanning positions: 15 × 19
X axis
Y axis

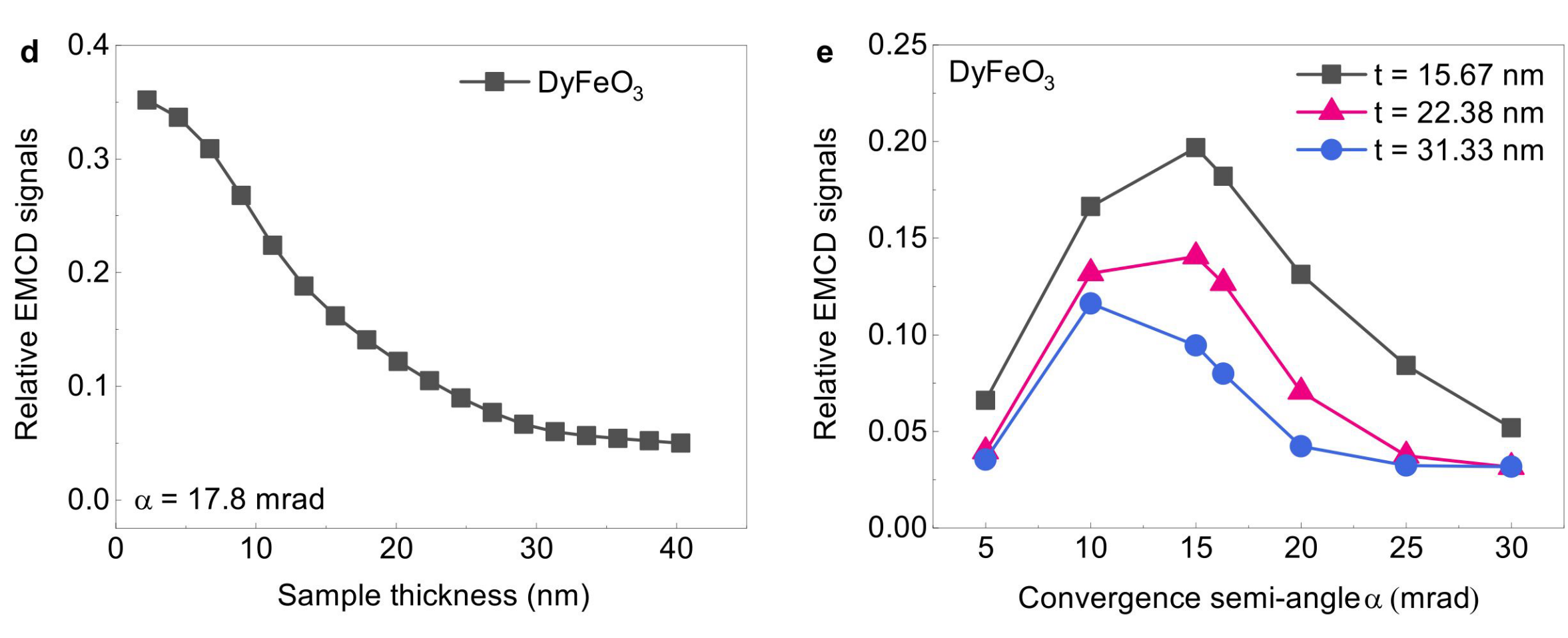

c
4.5
4
3.5
3
2.5
2
1.5
1
0.5
0


d
0.4
0.3
0.2
0.1
0
-0.1
-0.2
-0.3
-0.4


e
0.4
0.3
0.2
0.1
0
-0.1
-0.2
-0.3
-0.4

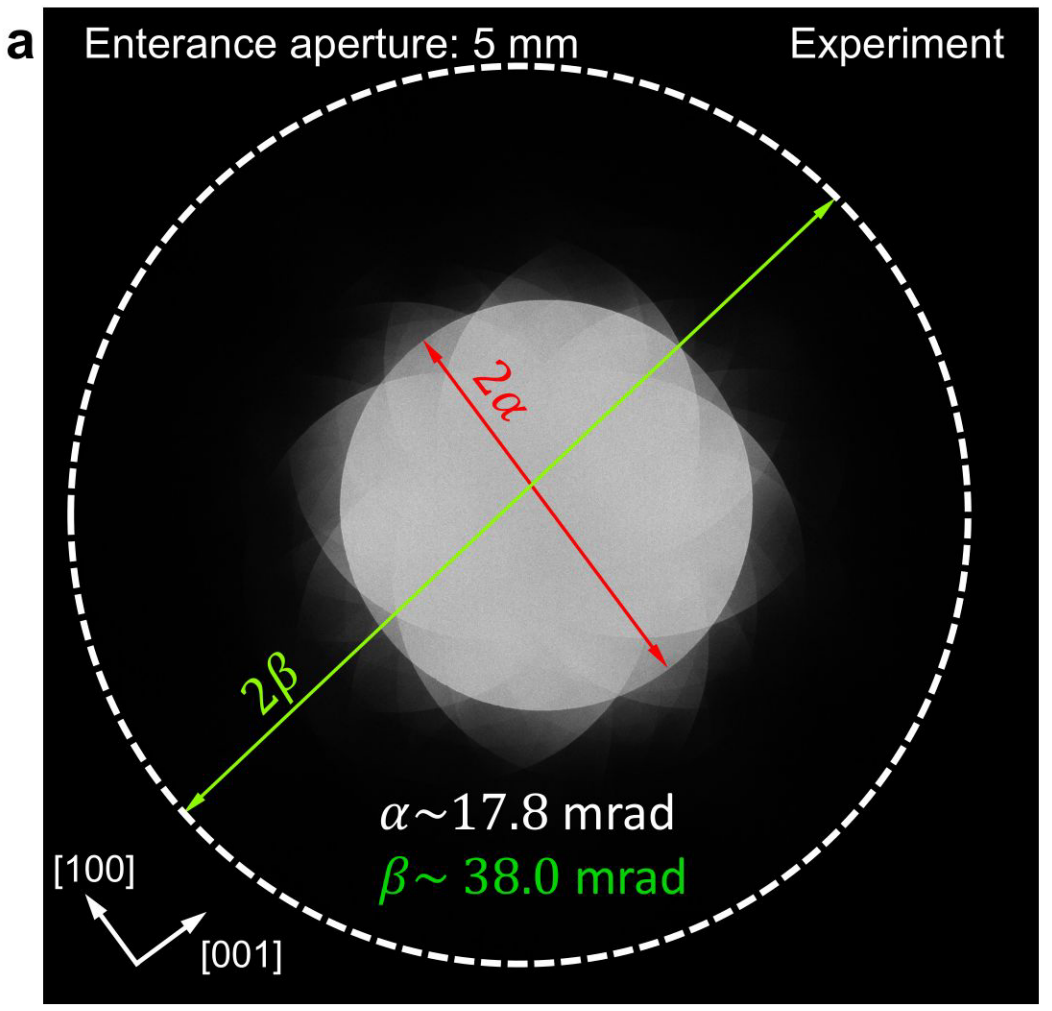

f
0.4
0.3
0.2
0.1
0
-0.1
-0.2
-0.3
-0.4

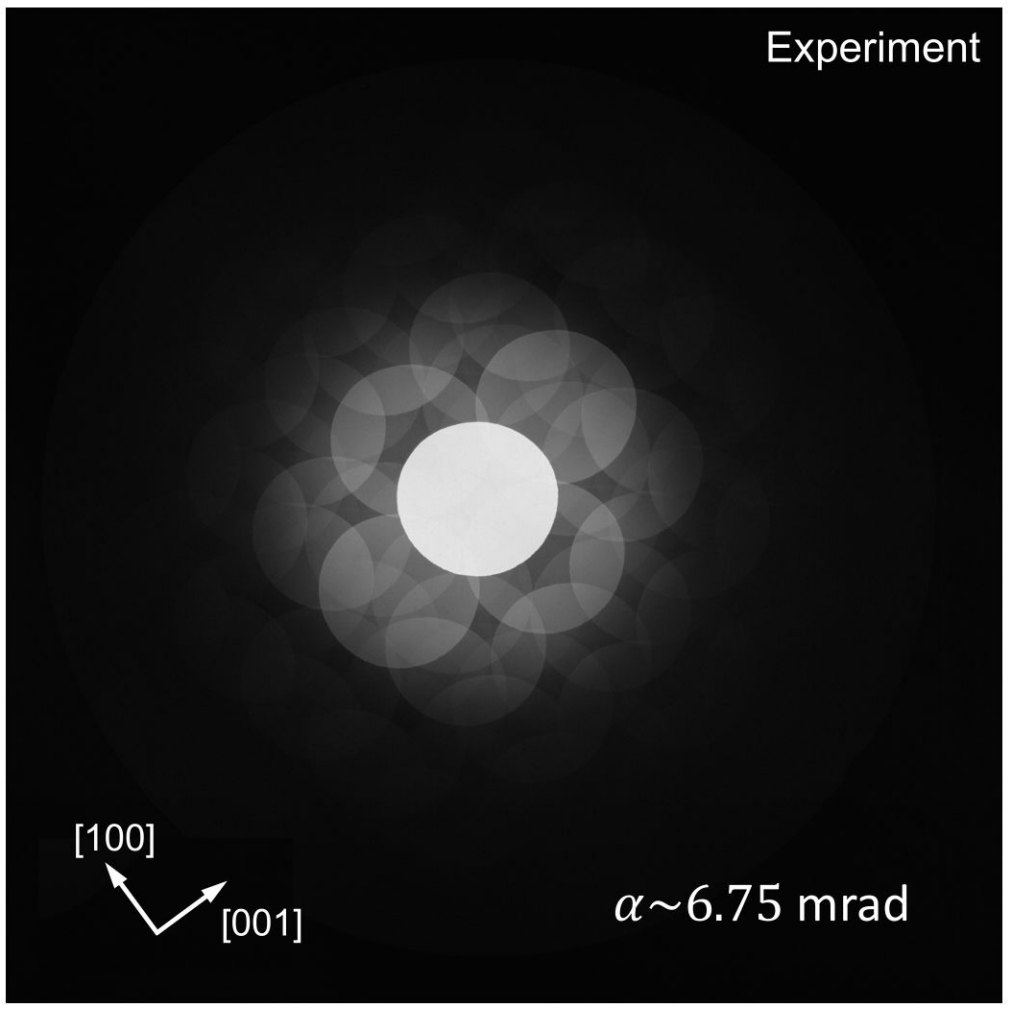

a
DyFeO3
Dy
Fe
Fe
O
y
x
z
b
CA = 10 mrad
CA = 15 mrad
CA = 17.8 mrad
CA = 20 mrad
CA = 25 mrad
Nonmag
600
400
200
0
c
EMCD
0.4
0.2
0
-0.2
-0.4

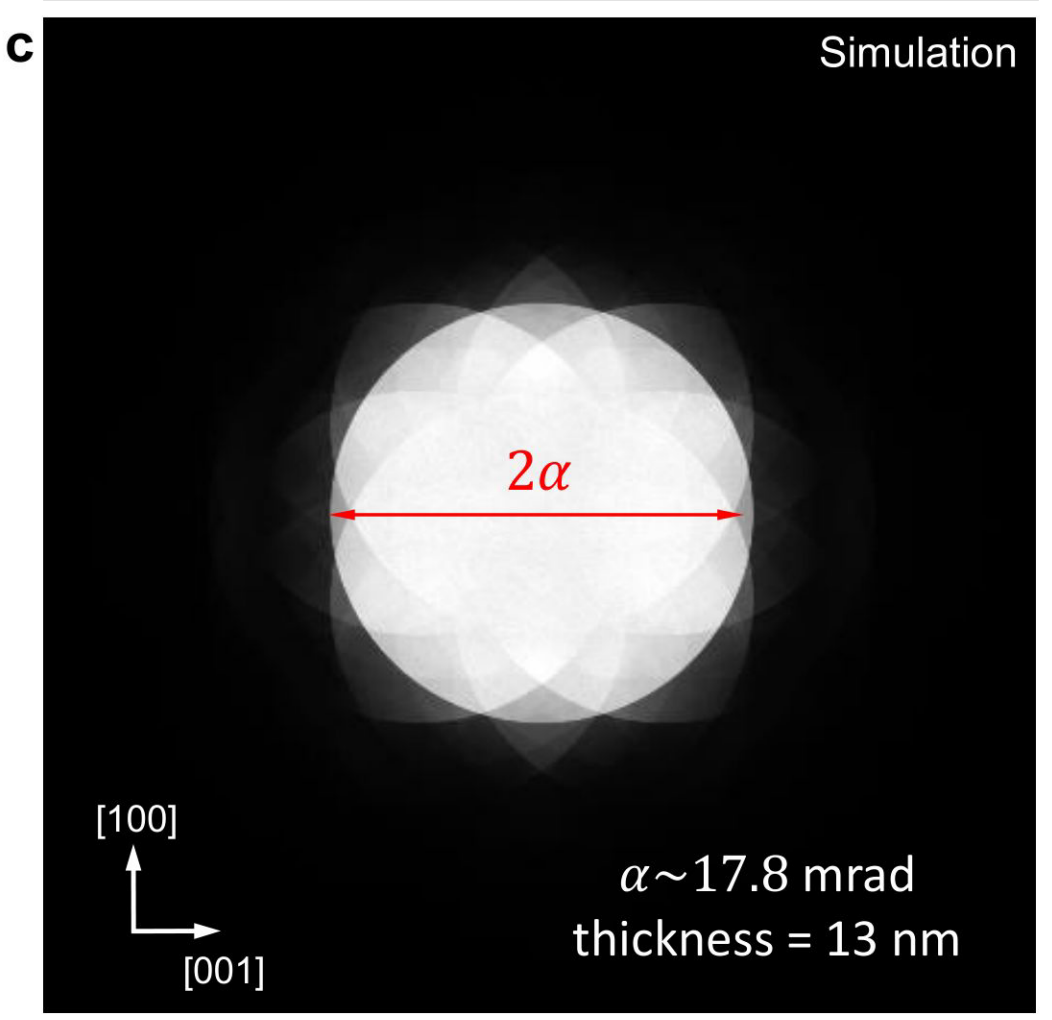

d
0.4
0.3
0.2
0.1
0.0
DyFeO3
α = 17.8 mrad
Relative EMCD signals
0
10
20
30
40
Sample thickness (nm)
e
0.25
0.20
0.15
0.10
0.05
0.00
DyFeO3
t = 15.67 nm
t = 22.38 nm
t = 31.33 nm
Relative EMCD signals
5
10
15
20
25
30
Convergence semi-angle α (mrad)

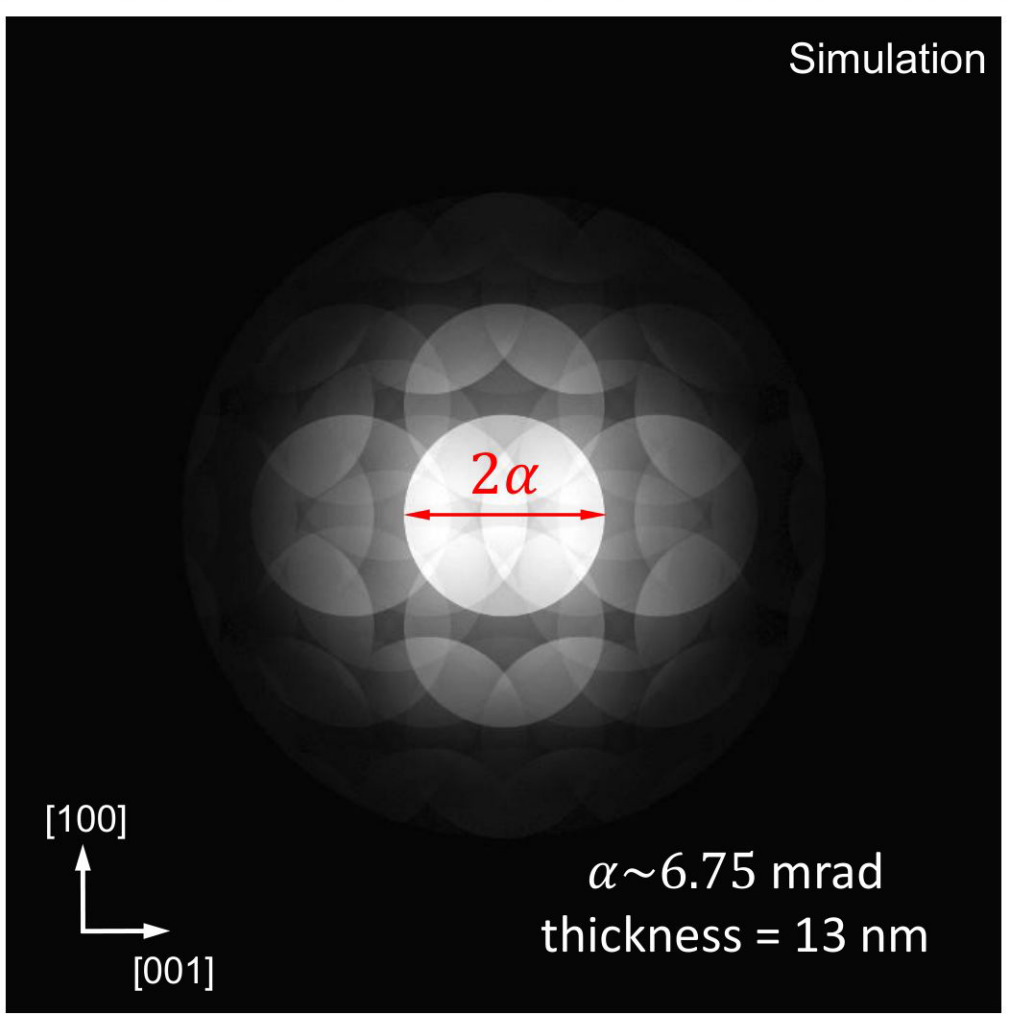
EMCD diffraction geometry

PACBED



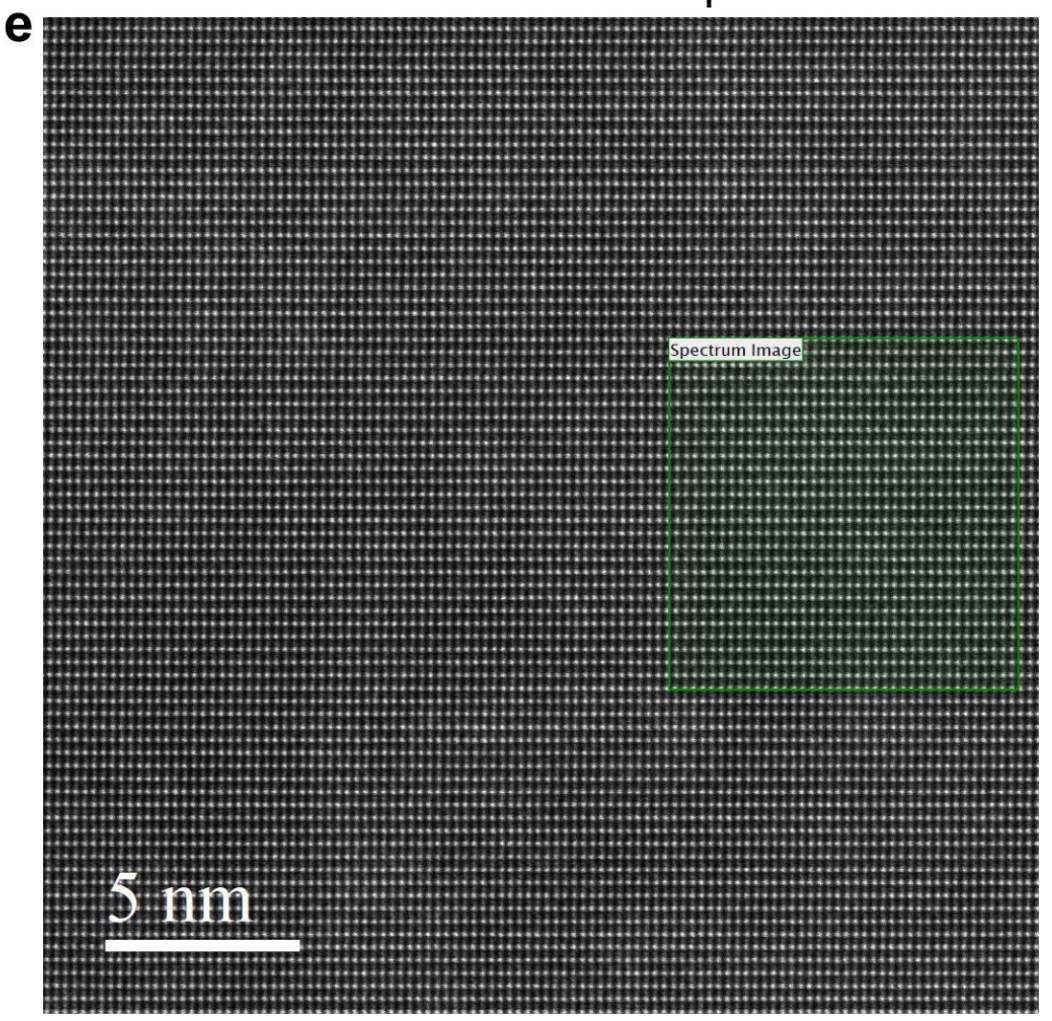


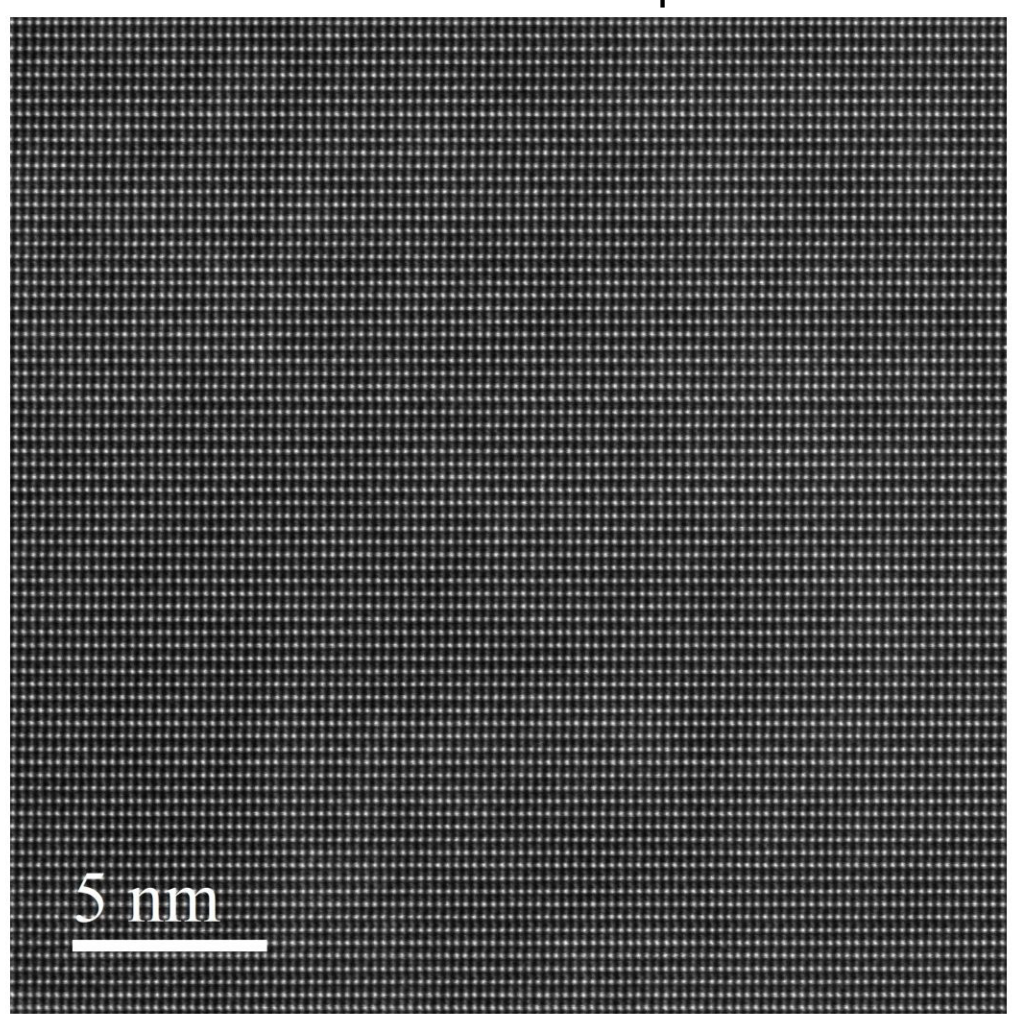




Before STEM-EELS experiments

After STEM-EELS experiments





Data Processing Procedures for Atomic-Resolution EMCD Signal Extraction

Pre-processing EELS data
(ADF image, LL, HL): energy calibration

Load Data
ADF image, HL_aligned

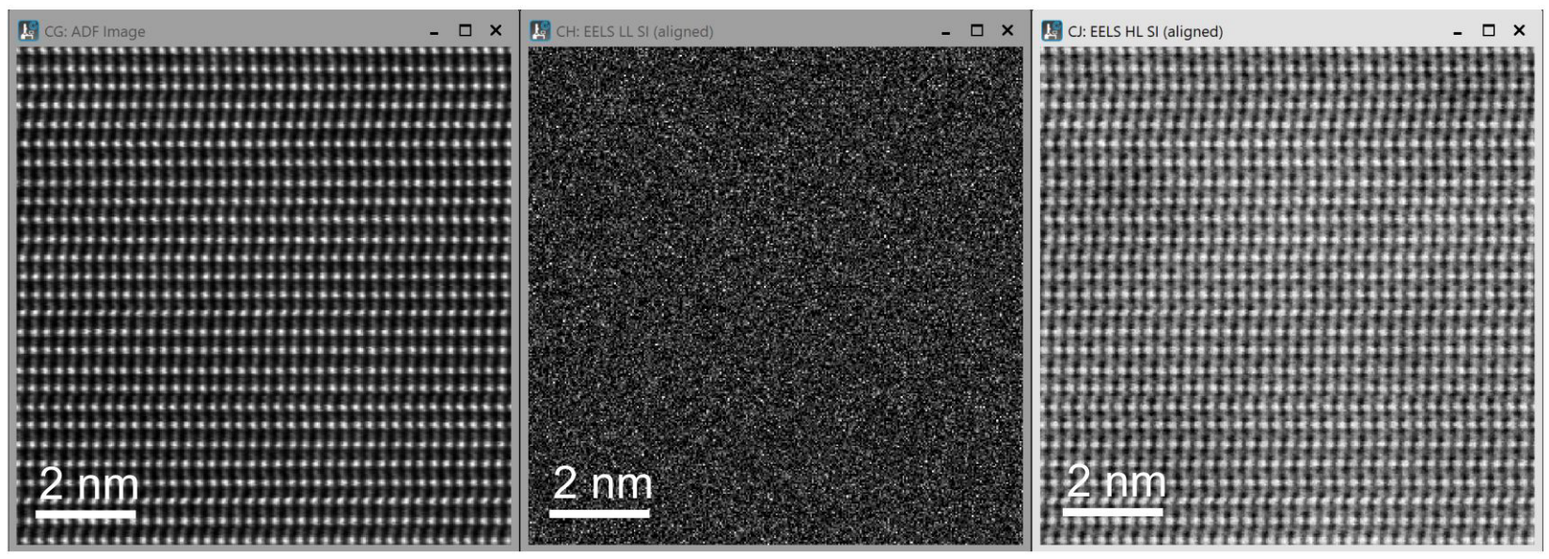
Find and index atom columns based on ADF image

Define ROI of chiral positions in real space for signal extraction based on ADF image

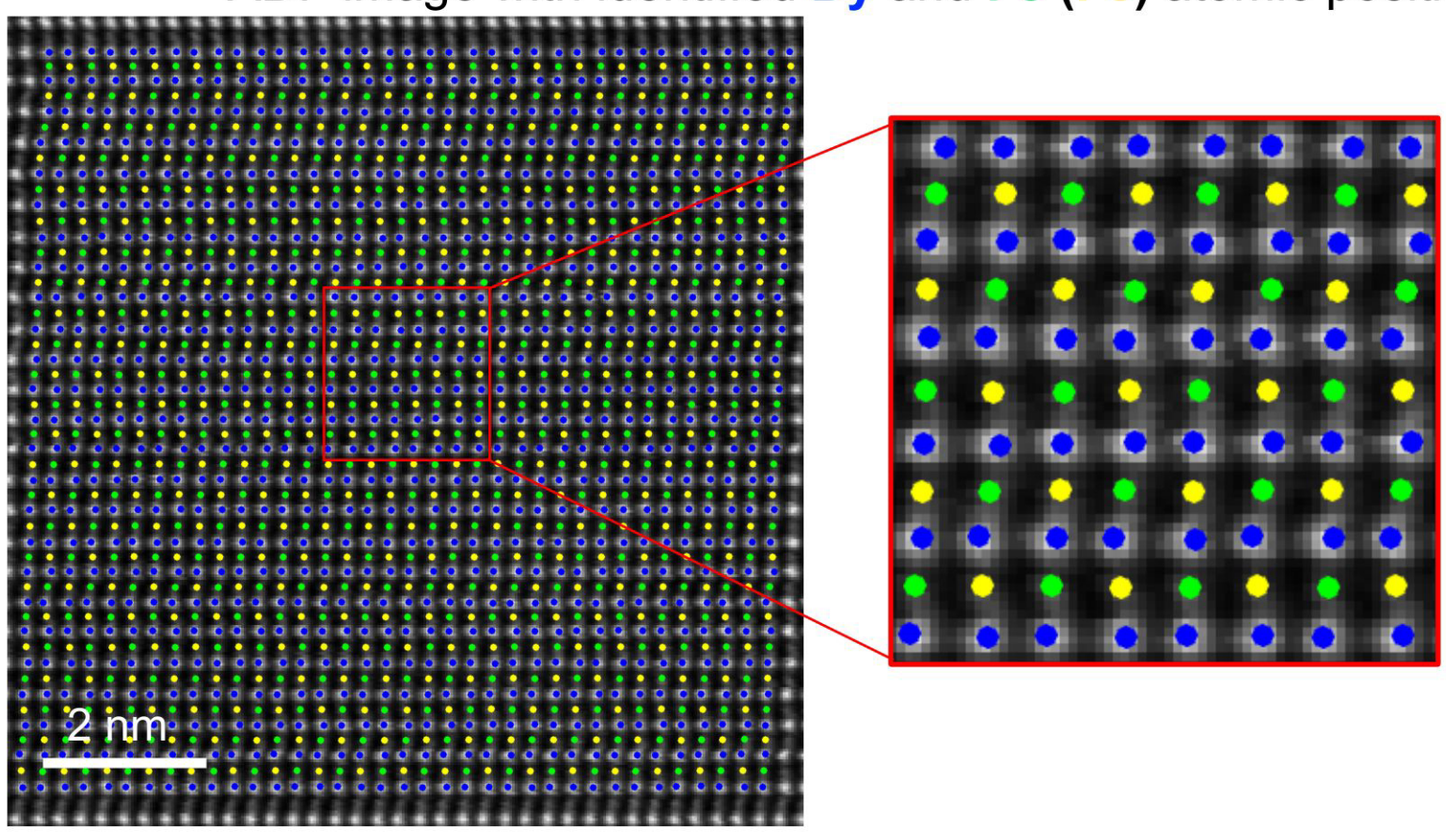
Apply ROI to HL_aligned
&
extract chiral+ and chiral– EELS signals

Post processing:
1. Averaged to obtain two chiral EELS
2. Background removal
3. Post-edge normalization
4. Calculate the difference

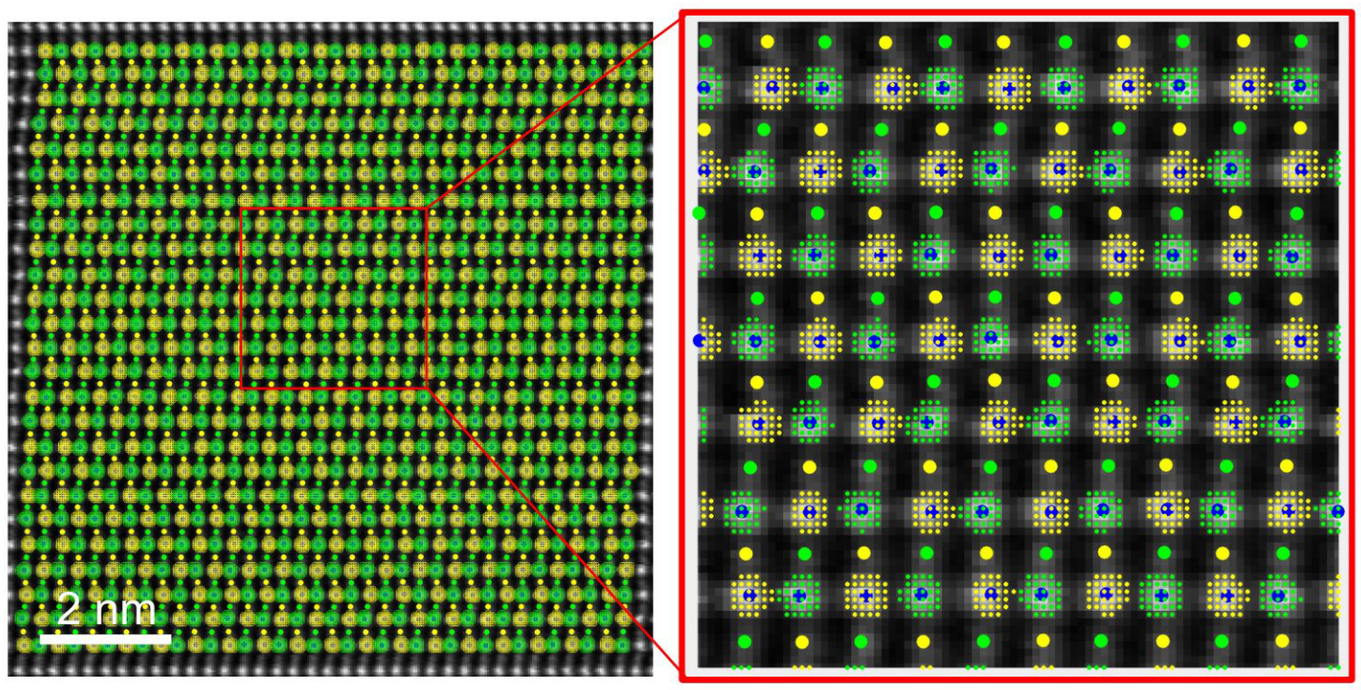
ADF image | Low-loss datacube | High-loss datacube

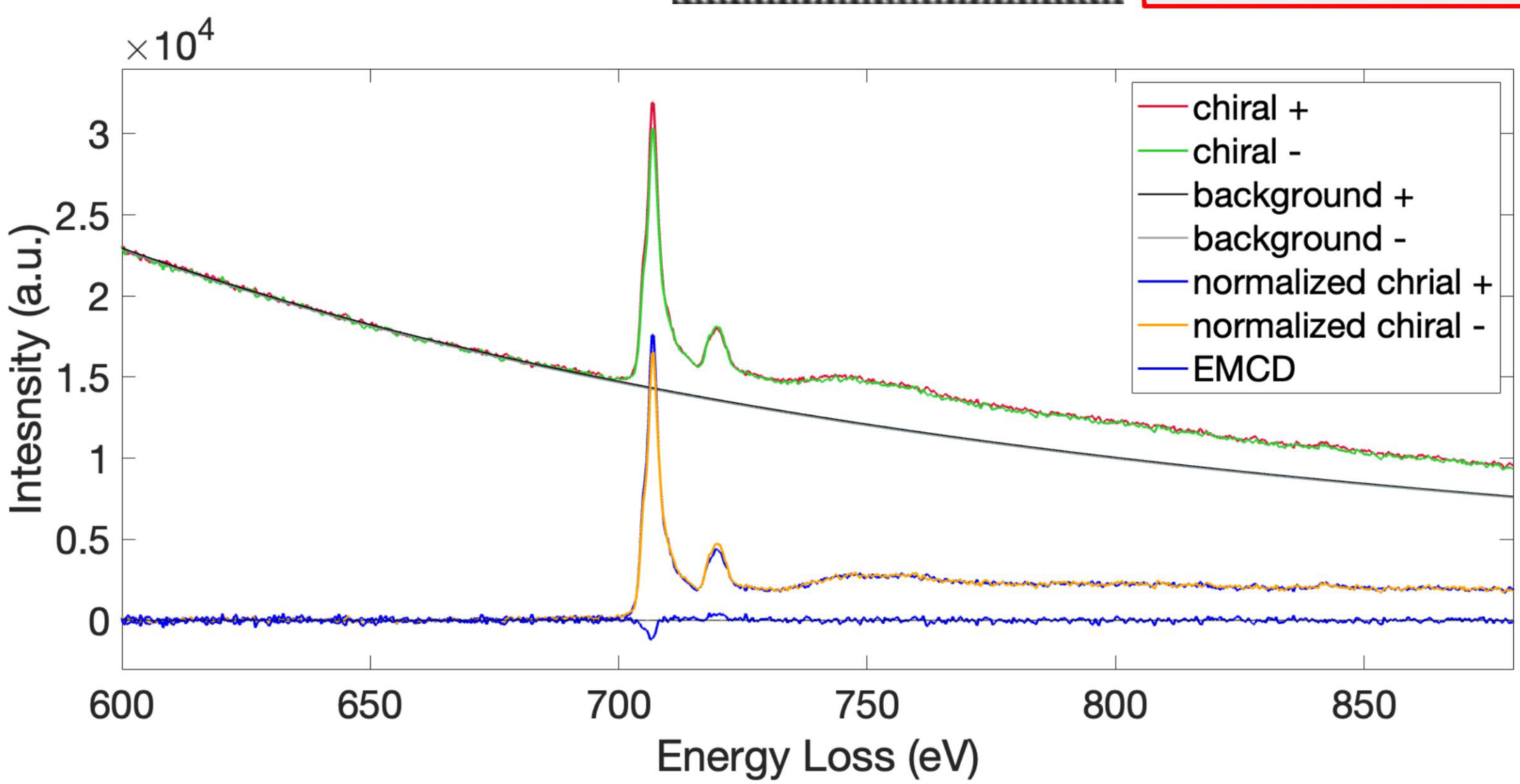


ADF image with identified Dy and Fe (Fe) atomic positions



ADF image with defined ROIs (chiral+ regions: small yellow points; chiral- regions: small green points) for EMCD signal extraction



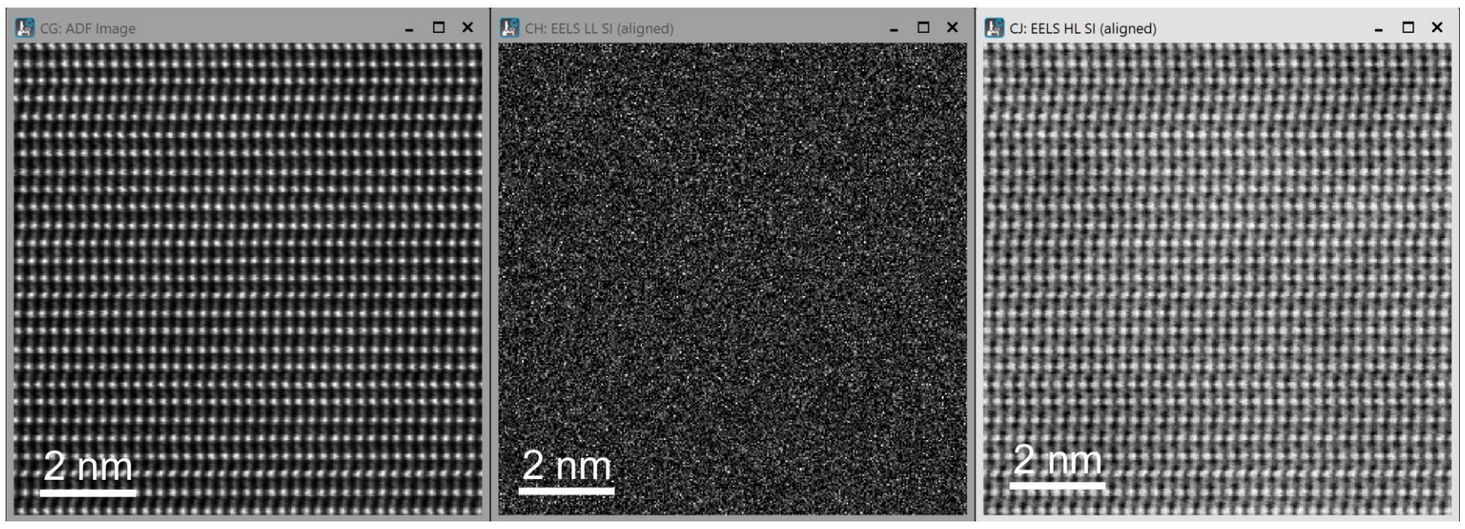


Data Processing Procedures for Atomic-Resolution EMCD Signal Mapping

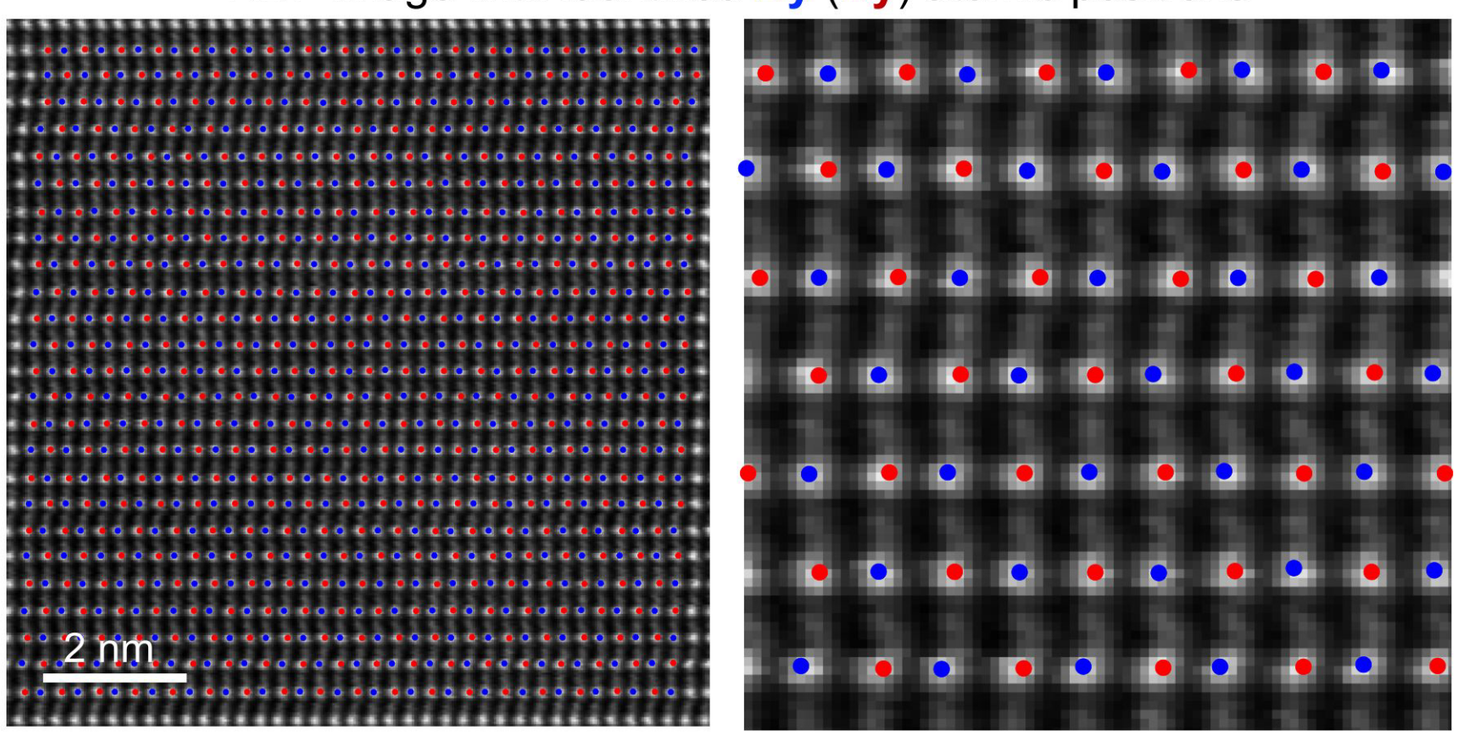
ADF image (size: 300×302)

Low-loss datacube (size: 300×302×3450)

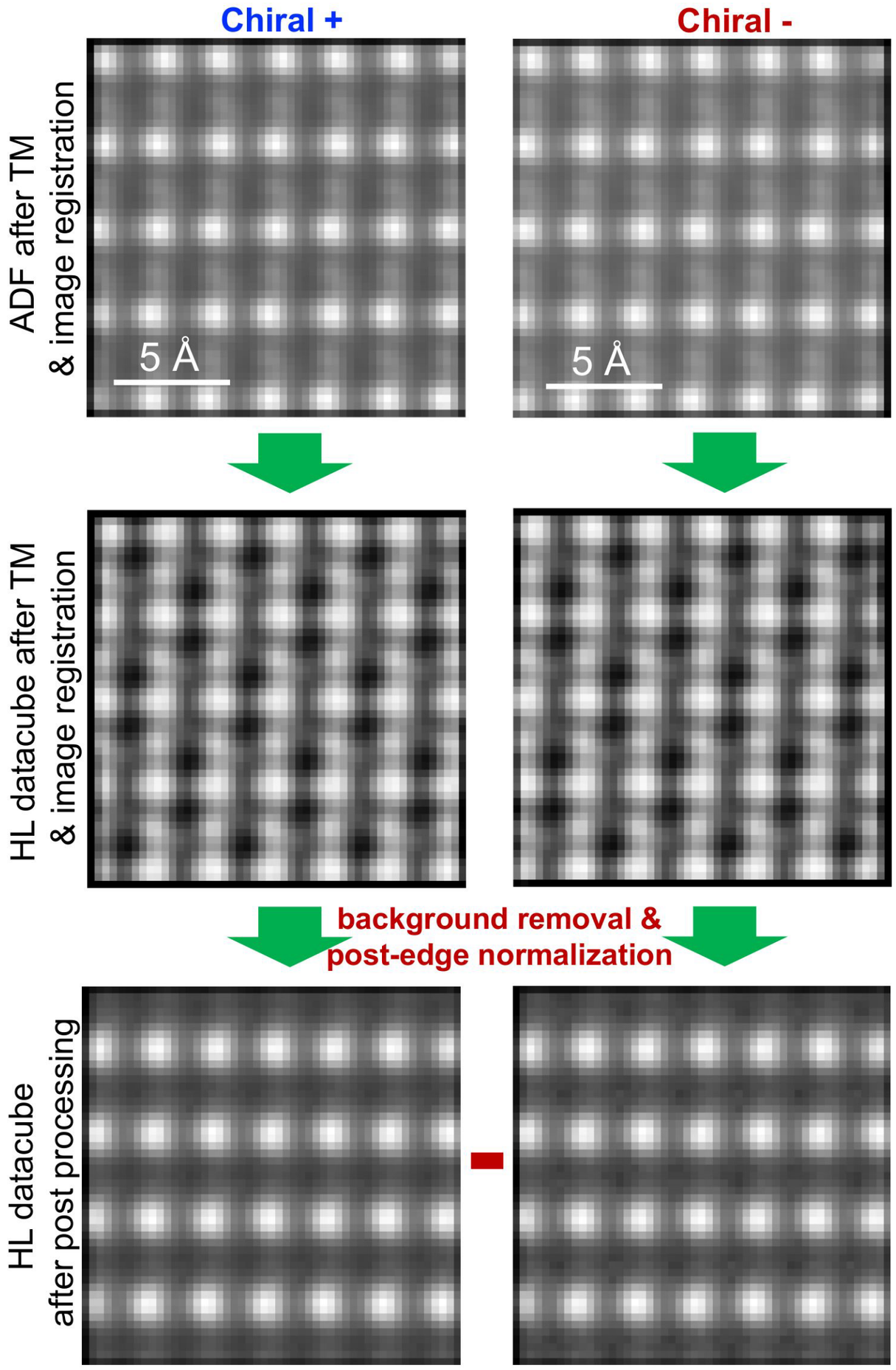
Hogh-loss datacube (size: 300×302×3450)



ADF image with identified **Dy** (**Dy**) atomic positions



Creating two chiral+/chiral- ADF image stacks based on the ROIs, which are defined by taking the center of **Dy** (**Dy**) atom positions with a size of 50×50 pixel



Pre-processing EELS data

(ADF image, Low-loss (LL) datacube, High-loss (HL) datacube): energy calibration

Load Data

ADF image, HL_aligned

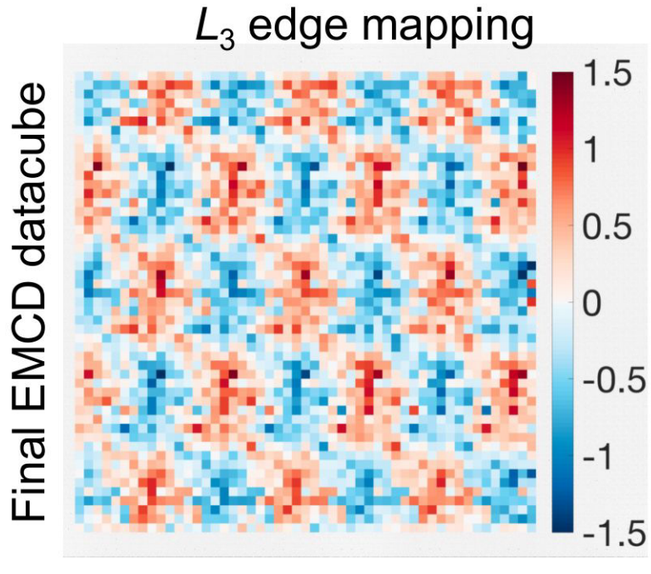
Find and index Dy atom positions based on ADF image

1. Define chiral+/chiral- ROI (size: 50×50 pixel) by taking the center of **Dy** (**Dy**) atom positions;
2. Obtain two ADF image stack: chiral+ ADF and chiral- ADF

1. Align the images in two ADF stacks and obtain two averaged ADF images;
2. Apply these procedures to HL_aligned stack and obtain two averaged EELS datacube (chiral+ and chiral-)

Post processing:

1. Background removal;
2. Post-edge normalization;
3. Calculate the difference between the two EELS datacube and obtain the EMCD datacube;



Dy(Sm)FeO_3

$\vec{M}//\vec{x}$

$\vec{M}//\vec{y}$

$\vec{M}//\vec{z}$

a

b

c

d

Dy
Fe
Fe
O

y
z
x

Nonmag

EMCD (x)

EMCD (y)

EMCD (z)

e

f

g

h

$DyFeO_3$

1000
800
600
400
200
0

0.2
0.1
0
-0.1
-0.2

0.05
0
-0.05

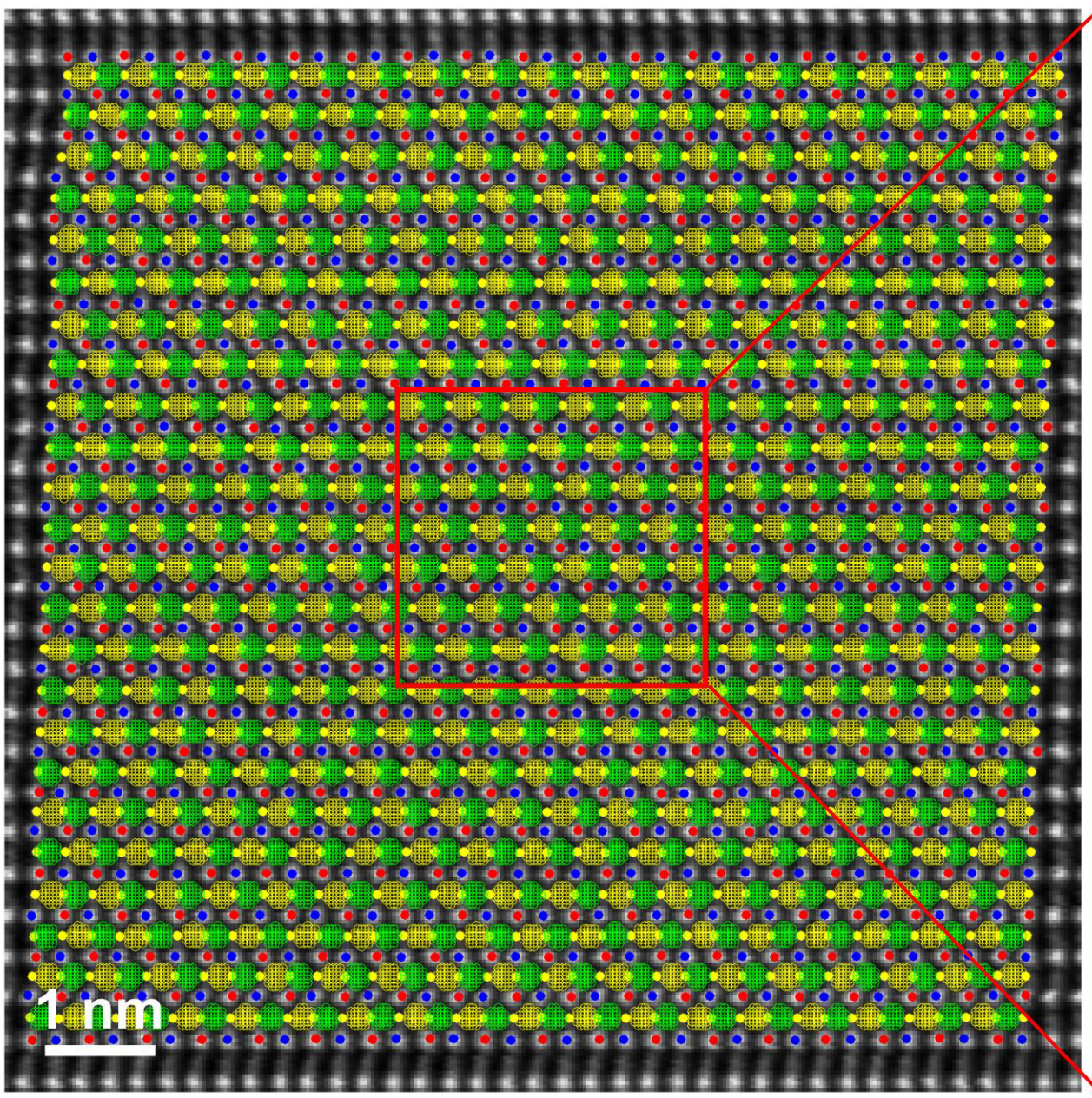
i

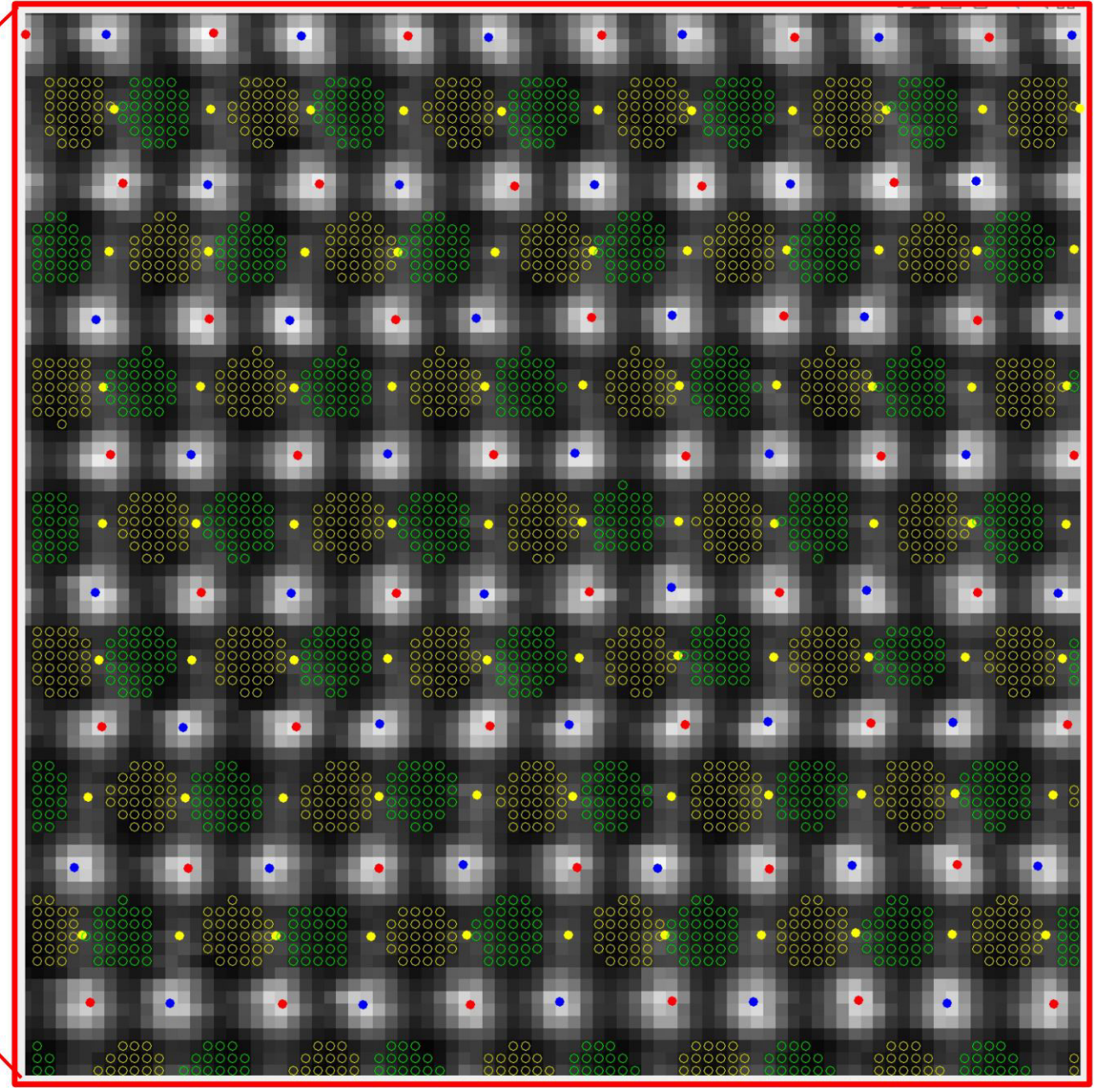
j

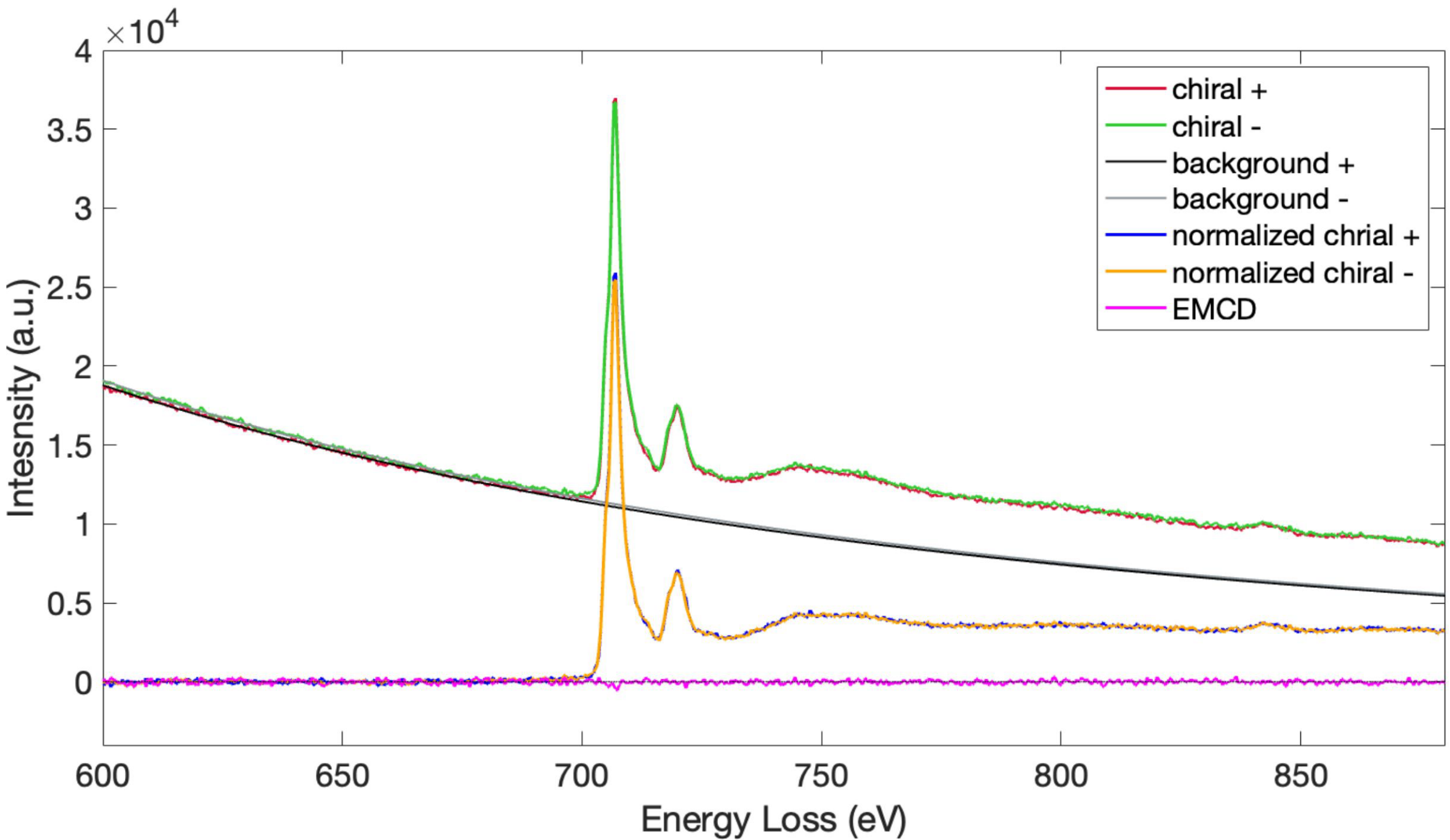
k

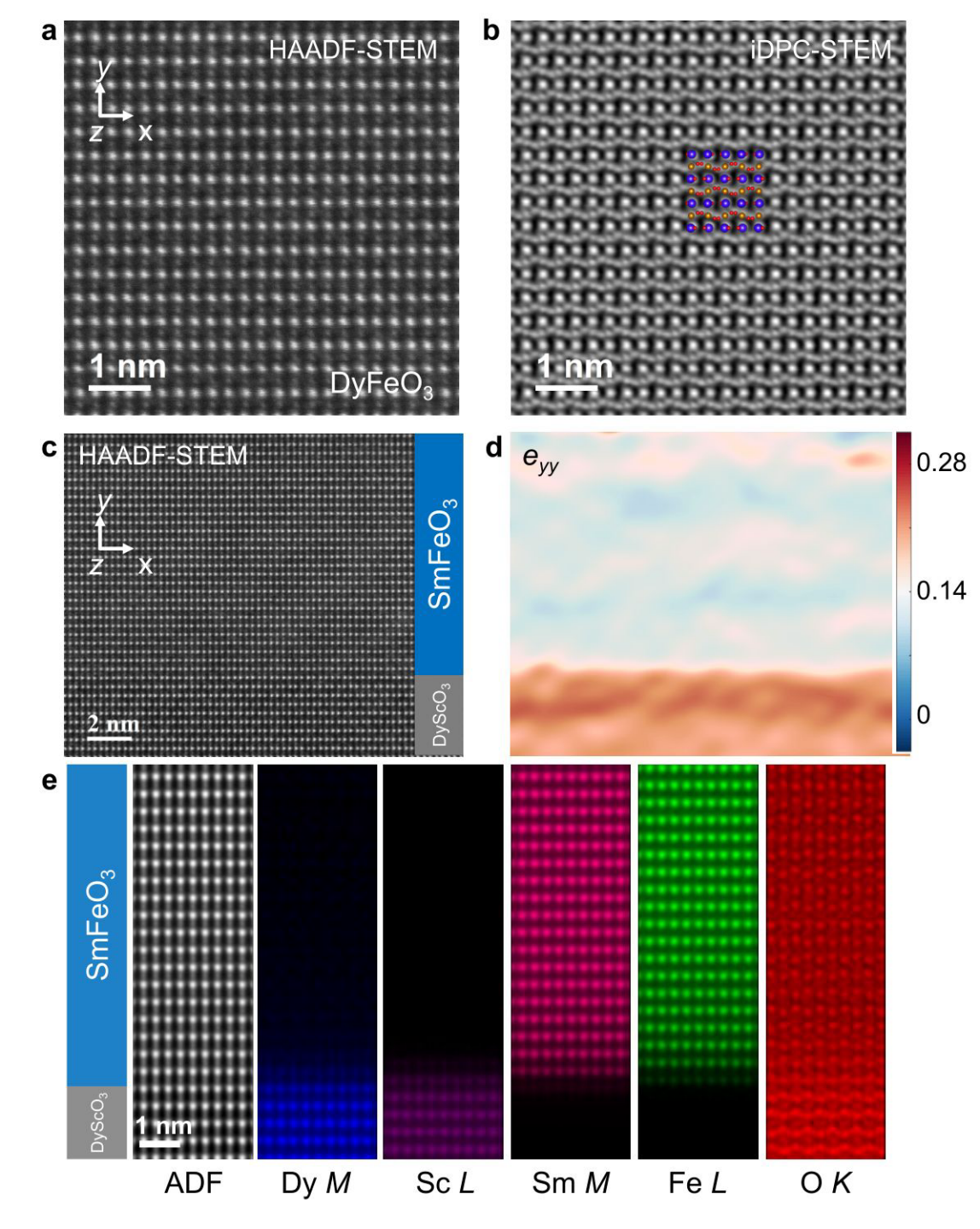
l

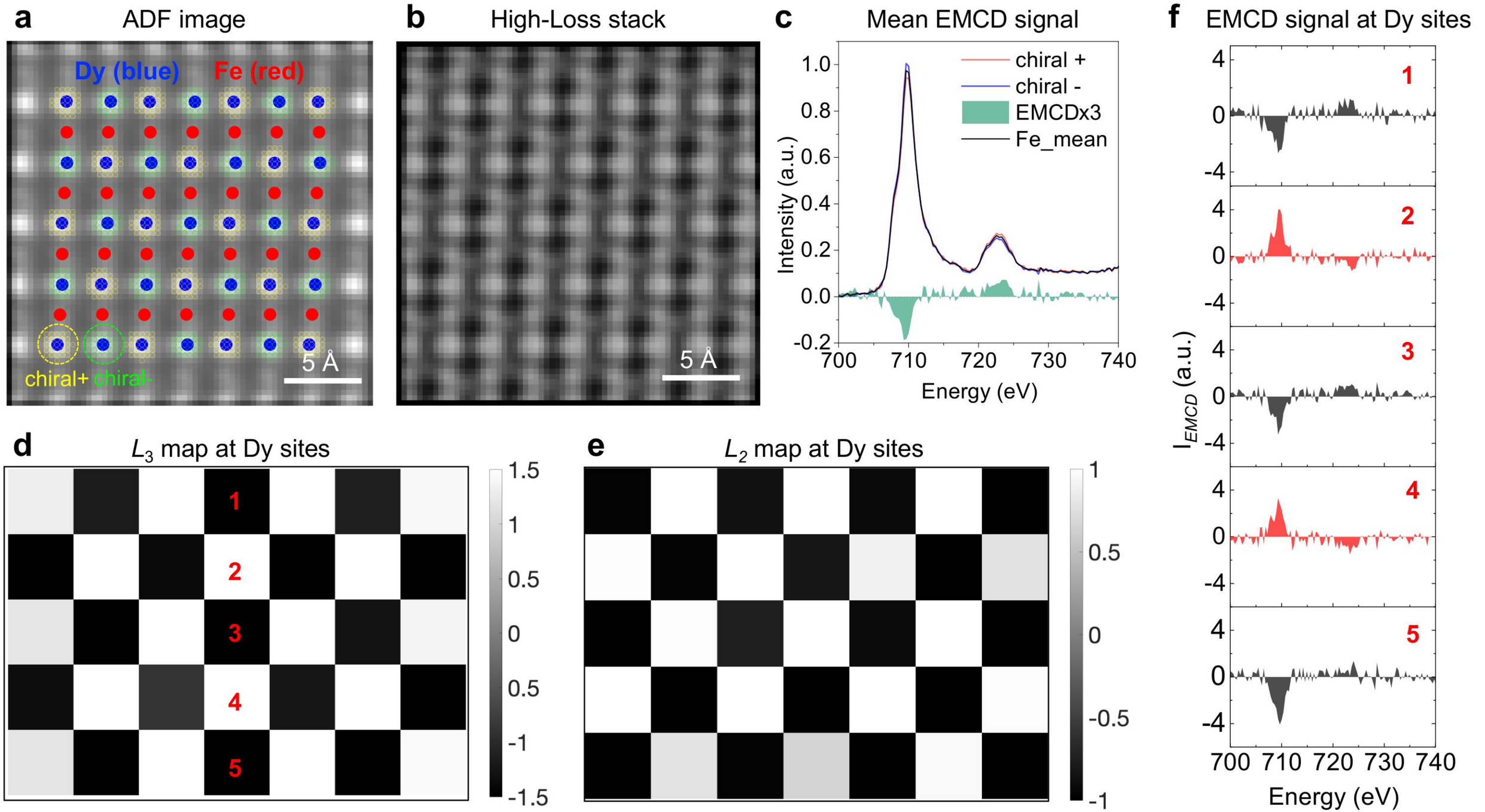
$SmFeO_3$


1 nm




×10^4
4
3.5
3
2.5
2
1.5
1
0.5
0
Intesnsity (a.u.)
600
650
700
750
800
850
Energy Loss (eV)
chiral +
chiral -
background +
background -
normalized chrial +
normalized chiral -
EMCD


a
HAADF-STEM
y
z
x
1 nm
DyFeO3
b
iDPC-STEM
1 nm
c
HAADF-STEM
y
z
x
SmFeO3
DyScO3
2 nm
d
eyy
0.28
0.14
0
e
SmFeO3
DyScO3
1 nm
ADF
Dy M
Sc L
Sm M
Fe L
O K


a
ADF image
Dy (blue)
Fe (red)
5 Å
chiral+
chiral-
b
High-Loss stack
5 Å
c
Mean EMCD signal
chiral +
chiral -
EMCDx3
Fe_mean
Intensity (a.u.)
Energy (eV)
f
EMCD signal at Dy sites
1
2
3
4
5
I_{EMCD} (a.u.)
Energy (eV)
d
L_3 map at Dy sites
e
L_2 map at Dy sites